

Machine learning Hubbard parameters with equivariant neural networks

Martin Uhrin^{1,2,*}, Austin Zadoks¹, Luca Binci^{1,3,4}, Nicola Marzari^{1,5}, and Iurii Timrov^{1,5,+}

¹Theory and Simulation of Materials (THEOS), and National Centre for Computational Design and Discovery of Novel Materials (MARVEL), École Polytechnique Fédérale de Lausanne (EPFL), CH-1015 Lausanne, Switzerland

²Université Grenoble Alpes, 1130 Rue de la Piscine, BP 75, 38402 St Martin D'Herès, France

³Department of Materials Science and Engineering, University of California at Berkeley, Berkeley, California 94720, United States

⁴Materials Sciences Division, Lawrence Berkeley National Laboratory, Berkeley, CA, 94720, USA

⁵Laboratory for Materials Simulations (LMS), Paul Scherrer Institut (PSI), CH-5232 Villigen PSI, Switzerland

*Email: martin.uhrin@grenoble-inp.fr

+Email: iurii.timrov@psi.ch

ABSTRACT

Density-functional theory with extended Hubbard functionals (DFT+ $U+V$) provides a robust framework to accurately describe complex materials containing transition-metal or rare-earth elements. It does so by mitigating self-interaction errors inherent to semi-local functionals which are particularly pronounced in systems with partially-filled d and f electronic states. However, achieving accuracy in this approach hinges upon the accurate determination of the on-site U and inter-site V Hubbard parameters. In practice, these are obtained either by semi-empirical tuning, requiring prior knowledge, or, more correctly, by using predictive but expensive first-principles calculations. Here, we present a machine learning model based on equivariant neural networks which uses atomic occupation matrices as descriptors, directly capturing the electronic structure, local chemical environment, and oxidation states of the system at hand. We target here the prediction of Hubbard parameters computed self-consistently with iterative linear-response calculations, as implemented in density-functional perturbation theory (DFPT), and structural relaxations. Remarkably, when trained on data from 11 materials spanning various crystal structures and compositions, our model achieves mean absolute relative errors of 3% and 5% for Hubbard U and V parameters, respectively. By circumventing computationally expensive DFT or DFPT self-consistent protocols, our model significantly expedites the prediction of Hubbard parameters with negligible computational overhead, while approaching the accuracy of DFPT. Moreover, owing to its robust transferability, the model facilitates accelerated materials discovery and design via high-throughput calculations, with relevance for various technological applications.

INTRODUCTION

A fundamental tool in investigating compounds involving transition-metal (TM) and rare-earth (RE) compounds is density-functional theory (DFT),^{1,2} a cornerstone for first-principles simulations in physics, chemistry, and materials science. In practical applications, DFT necessitates approximations to the exchange-correlation (xc) functional, with the local spin-density approximation (LSDA) and spin-polarized generalized-gradient approximation (σ -GGA) being the most prevalent choices. However, these approximations yield unsatisfactory outcomes for various properties of TM and RE compounds, primarily due to significant self-interaction errors (SIEs)³⁻⁵ that are particularly pronounced for localized d and f electrons. To address these challenges, more accurate approaches surpassing the limitations of “standard DFT” have been devised. Noteworthy among these are Hubbard-corrected DFT (so-called DFT+ U ⁶⁻⁸ and its extension DFT+ $U+V$,⁹⁻¹¹ whose role in addressing SIEs, rather than correlation errors, was first pointed out in Ref. 4), meta-GGA functionals,¹²⁻¹⁴ and hybrid functionals.¹⁵⁻¹⁷ While these methods offer valuable insights, each comes with inherent limitations and challenges, as discussed in, e.g., Ref. 18.

Hubbard-corrected DFT in particular stands out for its greater accuracy with only a marginal increase in computational cost over standard DFT functionals.²⁰ In the DFT+ $U+V$ scheme, a corrective Hubbard energy E_{U+V} is introduced alongside the approximate DFT energy E_{DFT} :

$$E_{\text{DFT}+U+V} = E_{\text{DFT}} + E_{U+V}. \quad (1)$$

In the simplified rotationally-invariant formulation,⁸ the extended Hubbard correction energy for a manifold with angular momentum ℓ takes the form:²¹

$$E_{U+V} = \frac{1}{2} \sum_{I\sigma} U^I \text{Tr} [\mathbf{n}_\ell^I (1 - \mathbf{n}_\ell^{I\sigma})] - \frac{1}{2} \sum_I \sum_{J(J \neq I)}^* \sum_{\sigma} V^{IJ} \text{Tr} [\mathbf{n}_\ell^{IJ\sigma} \mathbf{n}_\ell^{I\sigma}], \quad (2)$$

where I and J are atomic site indices, while m and m' denote magnetic quantum numbers associated with a specific angular momentum. U^I and V^{IJ} are effective on-site and inter-site Hubbard parameters, respectively. The asterisk in the sum signifies that, for each atom I , the index J encompasses all its neighbors up to a given distance. The generalized occupation

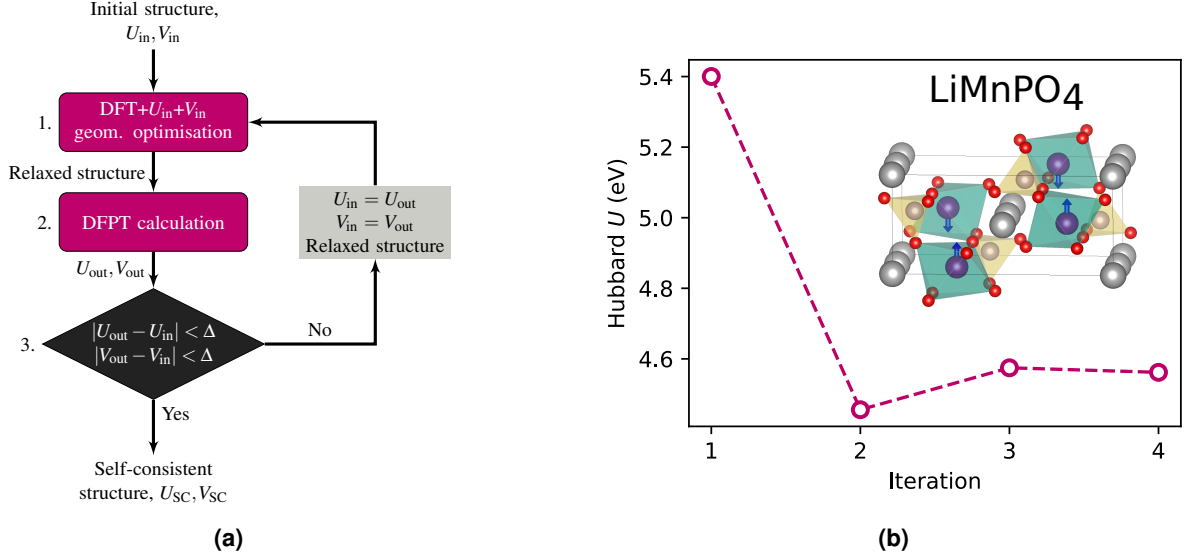


Figure 1. (a) Protocol for the self-consistent calculation of Hubbard parameters using density-functional perturbation theory (DFPT).¹⁹ U_{in} and V_{in} represent the input Hubbard parameters, while U_{out} and V_{out} denote the output parameters, with Δ representing the convergence threshold. U_{SC} and V_{SC} are the final self-consistent (SC) Hubbard parameters. (b) Convergence of the Hubbard U parameter for Mn-3d states in LiMnPO_4 using the self-consistent protocol.¹⁸ The inset displays the crystal structure of the material, where arrows indicate the spin direction, and Li atoms are depicted in grey, O in red, Mn in violet, and P in yellow.

matrices $\mathbf{n}_\ell^{IJ\sigma}$ are derived from the projection of the Kohn-Sham (KS) states onto localized atom-centered orbitals $\phi_m^I(\mathbf{r})$ (Hubbard projector functions) of neighboring atoms:

$$\mathbf{n}_\ell^{IJ\sigma} \equiv n_{mm'}^{IJ\sigma} = \sum_{\nu, \mathbf{k}} f_{\nu, \mathbf{k}}^\sigma \langle \psi_{\nu, \mathbf{k}}^\sigma | \phi_{m'}^J \rangle \langle \phi_m^I | \psi_{\nu, \mathbf{k}}^\sigma \rangle, \quad (3)$$

where ν and σ represent the band and spin labels of the KS wavefunctions $\psi_{\nu, \mathbf{k}}^\sigma(\mathbf{r})$, respectively, \mathbf{k} denotes points in the first Brillouin zone (BZ), and $f_{\nu, \mathbf{k}}^\sigma$ are the occupations of the KS states. The two terms in eq. (2) — proportional to on-site U^I and inter-site V^{IJ} — counteract one another. The on-site term promotes localization on atomic sites, suppressing hybridization with neighbors, while the inter-site term favors hybridized states with components on neighboring atoms. Consequently, the values of U^I and V^{IJ} are critical to optimizing the extent of the localization and hybridization within Hubbard-corrected DFT. However, these parameters are not known *a priori* and must be determined in some way. In passing we note that for the sake of simplicity, hereafter we drop the superscripts I and J in the notations of Hubbard parameters and occupation matrices, unless required for clarity.

Hubbard U can be fit semi-empirically to reproduce a target property from experimental data^{22–26} or from other advanced first-principles methods (e.g. GW ²⁷ or hybrids^{15–17}); however, this approach has many limitations. Fitted parameters are not guaranteed to, and often do not, accurately predict properties other than that used in fitting, and calibrating a single Hubbard U to multiple properties is non-trivial, requiring advanced algorithms like Bayesian optimization (BO).^{28,29} This method also precludes materials discovery, where properties are by

definition unknown, and targeting results of advanced first-principles methods, like DFT with hybrid functionals, inherits the limitations of those methods.^{30,31} Moreover, the inter-site V parameters, which are necessary to properly describe materials with pronounced covalent interactions, are difficult to fit semi-empirically due to the high-dimensional regression procedure they would require. An attractive alternative is computing Hubbard parameters using first-principles methods such as constrained DFT (cDFT),^{32–40} Hartree-Fock-based approaches,^{10,11,41–44} and the constrained random-phase approximation (cRPA).^{45–48} These methods do not rely on data from experiments or advanced simulation methods and, moreover, are able to provide values not only for U but also for V . However, first-principles approaches are considerably more computationally expensive than DFT+ U (+ V) ground-state calculations themselves, making their application feasible but demanding for large systems or high-throughput studies.

The linear-response (LR) formulation of cDFT (LR-cDFT)²¹ has witnessed popularity due to its simplicity and accuracy; however, it demands computationally expensive supercell calculations. A recent reformulation of LR-cDFT in terms of DFPT^{19,49} significantly reduces the computational burden for determining Hubbard parameters by replacing cumbersome supercell calculations with faster unit-cell calculations and by leveraging symmetries that further diminishes the computational cost by reducing the number of perturbations in reciprocal space (see Sec. S1 in the supplemental information (SI)). Its physical rationale relies on heuristically imposing piecewise linearity of the energy of the system as a function

of the population of the Hubbard manifold.²¹ Despite the numerous successful applications of DFPT in computing Hubbard parameters,^{18,50–57} this approach introduces a significant overhead compared to DFT+ U + V ground-state calculations. Moreover, it has been shown that jointly optimizing Hubbard parameters and the crystal structure, rather than relying on the equilibrium geometry obtained using (semi-)local functionals, can significantly improve the accuracy of the final properties of interest.⁵⁸ This is due in part to taking into account the geometry dependence of $U\{\mathbf{R}\}$ and thus the contribution $dU/d\mathbf{R}$ to the Hellmann-Feynman forces.⁵⁹ To do so, a self-consistent procedure combining DFPT and structural optimizations (fig. 1a) can be used (see Sec. S2 in the SI).^{19,60} Figure 1b shows a typical self-consistent determination of Hubbard parameters for LiMnPO₄ following this procedure, where each iteration costs approximately one order of magnitude more computational time than a Hubbard-corrected DFT electronic ground-state calculation. Consequently, the adoption of acceleration techniques is highly sought after to expedite the determination of Hubbard parameters while providing a level of accuracy very close to that of DFPT and, prospectively, a simple estimate of $dU/d\mathbf{R}$ and $dV/d\mathbf{R}$.

The application of machine learning (ML) algorithms to predict Hubbard parameters is gaining popularity, as exemplified by a recent work, Ref. 61, which employs a random forest regression model. Ref. 61 uses crystal structure parameters, such as bond lengths and angles (among others), as descriptors for an ML model trained on a database of Mn oxides. In this study, the training data consist of U values fitted using Bayesian optimization to replicate band gaps and band structures obtained from HSE calculations — a concept initially proposed in the earlier work of Ref. 28 within the context of DFT+ U and subsequently extended to the DFT+ U + V framework.⁶² The resulting ML model predicts U values such that subsequent DFT+ U calculations using these values yield band gaps that are 2 – 3 times smaller than the reference HSE values, while the band structures appear qualitatively similar. Despite the significance of these efforts in applying ML to the prediction of Hubbard parameters, numerous critical issues persist, such as the accuracy of the reference training data (HSE often provides unreliable band gaps for solids^{30,31}), the choice of the target properties for the training data (fitting U to reproduce band gaps is questionable), the importance of self-consistency between Hubbard parameters and the crystal structure, as well as the inclusion of inter-site V which has been neglected thus far, to name a few. Addressing these points is highly relevant and necessitates further investigation, which serves as the motivation for this work.

Here, we introduce a novel ML approach based on equivariant neural-networks (ENNs) which aims to replace computationally demanding first-principles DFPT calculations of Hubbard U and V parameters while providing a negligible loss of accuracy for the vast majority of practical applications. Crucially, the model employs: 1) atomic occupation matrices within the DFT+ U + V framework as descriptors of the geom-

etry, electronic structure (e.g. oxidation states (OSs) and local chemical environments in materials, as well as 2) DFPT-based Hubbard parameters, and 3) interatomic distances. This model is general and can be applied to materials with ionic, covalent, and mixed ionic-covalent interactions. It is trained on all intermediate Hubbard parameters and occupation matrices obtained during the self-consistent cycle and directly provides the final self-consistent values of U and V , thus also bypassing intermediate structural optimizations. The utilization of ENNs facilitates the exploitation of the inherent O(3) group structure of the occupation matrices, ensuring excellent model performance even with scarce training data. Equivariant models have demonstrated state-of-the-art accuracy and transferability in ML interaction potentials,^{63,64} while our work is the first to incorporate electronic-structure degrees of freedom as explicit features in solids.

RESULTS

Occupation matrices as the model inputs The goal of our ML approach is to replace the self-consistent procedure represented in fig. 1a and provide the final Hubbard parameters using as input results from an initial DFT(+ U + V) calculation. Conventional ML methods for atomistic systems primarily use the ionic structures as inputs (see e.g. Refs. 65–68), sidestepping the need to explicitly calculate or even consider the electronic structure. However, as a consequence such models may not be particularly sensitive to changes in electronic structure that only lead to subtle changes in local atomic geometry, as can happen during a change of OS. To overcome this limitation, our models take as input the on-site occupation matrices $\mathbf{n}_\ell^\sigma \equiv \mathbf{n}_\ell^{I\sigma}$ [see eq. (3), $I = J$], which describe the local electronic structure around an atom, including the OS which is reflected in the occupation matrix eigenvalues.⁶⁹ This is a particularly compelling choice given the significant variations in Hubbard parameters seen for different OSs of TM elements.^{18,52}

As with any learning task, the ML model should respect the way in which the target physical properties transform under global rotations, translations, reflections and permutations of labels. In the present case, the output U and V values are left unchanged by these transformations, however the entries of the occupation matrix *do* change under rotation, making $n_{mm'}^\sigma$ unsuitable for use as inputs to non-symmetry aware models. For this reason, we make use of an *equivariant* learning model,^{70–73} which has the property that the learned function $f : X \rightarrow Y$ obeys the following relation:

$$D_Y[g]f(x) = f(D_X[g]x), \quad \forall g \in G, \forall x \in X, \quad (4)$$

where the equivariance is with respect to a group G (in our case SE(3)), and $D_Y[g]$ and $D_X[g]$ are representations that act on the vector spaces Y and X , respectively. For example, applying a rotation to the inputs and then applying f must produce the same outputs as applying the rotation to the outputs of f given the original (unrotated) input. While

Attribute	Irreducible representation
U^I, V^{IJ}, r_{IJ}	$D^{(0,1)}$
Atomic species	$\bigoplus^{N_s} D^{(0,1)}$
\mathbf{n}_p^σ	$D^{(0,1)} \oplus D^{(2,1)}$
\mathbf{n}_d^σ	$D^{(0,1)} \oplus D^{(2,1)} \oplus D^{(4,1)}$

Table 1. Irreducible representations of various attributes (inputs and outputs) of the ML model. U^I and V^{IJ} are the on-site and inter-site Hubbard parameters, respectively, r_{IJ} is the interatomic distance between species I and J , N_s is the number of atomic species (one-hot vectors), \mathbf{n}_p^σ and \mathbf{n}_d^σ are the occupation matrices for the p and d orbitals, respectively, in the special representation for the ML model [see eqs. (5) and (6)]. The irreducible representations of the occupation matrices can be readily obtained using the e3nn^{73,75} library.

our model outputs scalars (which are symmetry invariant), by using an equivariant model we ensure that the inputs and all intermediate (hidden) features transform together under group actions. This property has been shown to give state-of-the-art accuracy and transferability, particularly within the domain of ML interaction potentials.^{63,68,74}

Equivariant descriptors By virtue of being atom-centred, the on-site occupation matrix \mathbf{n}_ℓ^σ is naturally invariant to global translations. However, to build a rotationally invariant model, it is convenient to re-express the occupation matrix in terms of the irreducible representations (irreps) of the O(3) group. If we let $D^{(\ell,P)}$ be the irrep with degree ℓ and parity P , we can express the occupation matrices as the tensor products $D^{(\ell,P)} \otimes D^{(\ell,P)}$, where e.g. $\ell = 1$ for p orbitals, and $\ell = 2$ for d orbitals. These can then be decomposed into a direct sum of irreps, e.g. for $\ell = 1$ and $P = -1$ the occupation matrix is a 3×3 , rank-2, tensor $D^{(1,-1)} \otimes D^{(1,-1)}$, that is symmetric, as $\mathbf{n}_\ell^\sigma = (\mathbf{n}_\ell^\sigma)^\top$. In practice, this decomposition is achieved by applying a change of basis for \mathbf{n}_ℓ^σ that transforms it into the irrep basis (see SI S3 for details). At this stage, the remaining symmetry to be addressed is that of label permutation. In the case of the atom labels for the inter-site term, the model should be invariant to permutation of I and J , however in our training data the Hubbard V correction is always applied to a d -block/ p -block atom pairs which have occupation matrices of different dimension (5×5 for d and 3×3 for p), thereby making them distinguishable.

There remains a permutational invariance to be imposed on the spin labels ($\sigma = \uparrow$ or \downarrow). We achieve this using permutationally invariant polynomials:

$$\mathbf{x}_\ell^1 = \mathbf{n}_\ell^\uparrow + \mathbf{n}_\ell^\downarrow, \quad (5)$$

$$\mathbf{x}_\ell^2 = \mathbf{n}_\ell^\uparrow \otimes \mathbf{n}_\ell^\downarrow. \quad (6)$$

In the following, for the sake of convenience, we label these tensors in their irrep form as \mathbf{x}_p^i for p orbitals and \mathbf{x}_d^i for d orbitals, where i can be 1 or 2. We note in passing that

in the non-spin-polarized case, one can set $\mathbf{n}_\ell^\uparrow = \mathbf{n}_\ell^\downarrow = \mathbf{n}_\ell/2$, where \mathbf{n}_ℓ is divided by two to account for spin degeneracy, and then proceed as above. In addition, atomic species (i.e. atomic types) are encoded as one-hot vectors in our ML model. For example, for a model that supports N_s distinct atomic species, we choose an arbitrary labelling of a N_s long vector, [Mn, Fe, Ni, O, ...], and place a 1 at the entry corresponding to the site element and zeros everywhere else (Mn = [1, 0, 0, 0, 0, ...], Fe = [0, 1, 0, 0, 0, ...], etc). A summary of the irreps of all the model inputs is presented in Table 1. In the case of the ML model for Hubbard V , the interatomic distances r_{IJ} are also included as an additional input, giving some basic information of the ionic structure.

Equivariant neural-network model To construct our ML model, we use the e3nn library^{73,75} and PyTorch;⁷⁶ our codebase is open-source and freely available (see *code availability* below). As shown in fig. 2, we define two separate models, one for predicting the on-site U values and the other for the inter-site V ones. By using separate models, we provide flexibility for the model to be used in calculations where only Hubbard U is applied (i.e. DFT+ U). In each case, the model starts with one or more nodes that carry attributes, expressed as a direct sum of irreps, which represent the inputs to the learned function. The inputs pass through a series of repeated layers made up of a tensor product (analogous to all-to-all connected layers in a traditional neural network) and a gated non-linearity (an equivariant version of a traditional activation function⁷⁵) followed by a final tensor product before readout. All of the tensor products have learnable weights, meaning that every pair of input irreps that contribute to one output irrep has a learnable scalar parameter that is optimised during training. We use the AdamW⁷⁷ optimiser to minimise the loss, which is the mean squared error between predicted and training Hubbard parameters.

Training and validation datasets To train and validate our ENN model, we curated a dataset comprising materials with diverse crystal structures. This dataset is constructed based on an investigation of various Li-ion cathode materials, covering olivine-type,¹⁸ spinel-type,⁵² and layered-type⁷⁸ structures at different Li concentrations, employing the self-consistent DFT+ U and DFT+ U + V protocols outlined above. Additionally, we include materials such as tunnel- and rutile-type MnO_2 ^{51,79} and perovskite-type rare-earth nickelates⁵³ in our dataset. The crystal and electronic structure details, magnetic ordering, and various other properties of these materials are extensively documented in their respective publications. These are the compounds containing TM elements Ni, Mn, and Fe, and a list of all these materials is provided in table 2. It is crucial to note that, while our current dataset is relatively small in terms of material count, ongoing efforts are directed towards a high-throughput exploration involving hundreds of materials, which will serve as an expanded training and validation set for our ENN model in the future. As a proof of concept, this initial dataset demonstrates the efficacy of

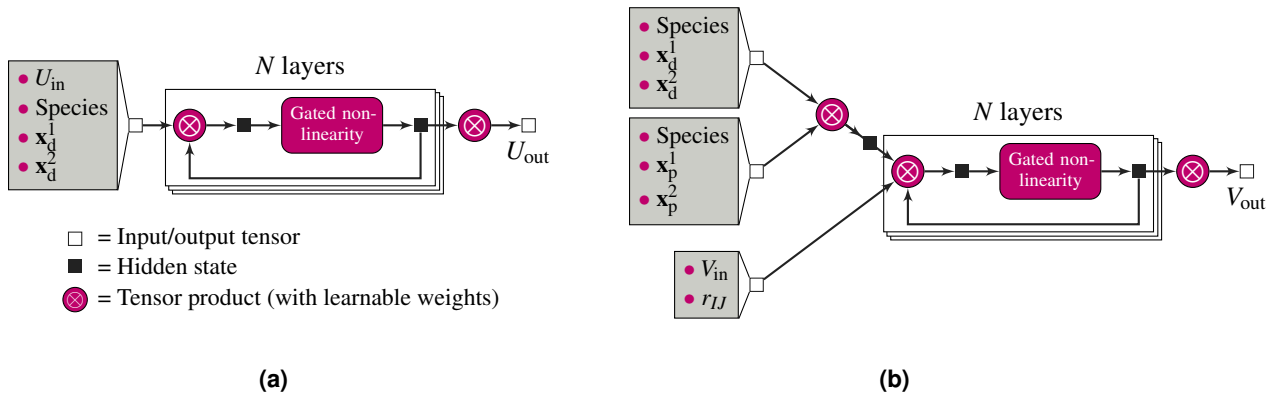


Figure 2. Schematic illustration of the equivariant neural-network ML model for predicting on-site Hubbard U (a) and inter-site Hubbard V (b) parameters. U_{in} and V_{in} are the input Hubbard parameters, while U_{out} and V_{out} are the outputs. The atomic species enter as one-hot tensors, and r_{IJ} is the interatomic distance between sites I and J . \mathbf{x}_d^1 and \mathbf{x}_d^2 are the occupation matrices for the d orbitals, while \mathbf{x}_p^1 and \mathbf{x}_p^2 for the p orbitals, all in the special representation for the ML model [see eqs. (5) and (6)]. Tensors are represented as squares: open for inputs and outputs, and filled for intermediate features.

Crystal structure type	Chemical composition	#
Olivine	Li_xFePO_4	5
	Li_xMnPO_4	5
	$\text{Li}_x\text{Fe}_{0.5}\text{Mn}_{0.5}\text{PO}_4$	5
Spinel	$\text{Li}_x\text{Mn}_2\text{O}_4$	2
	$\text{Li}_x\text{Mn}_{1.5}\text{Ni}_{0.5}\text{O}_4$	2
Layered	Li_xNiO_2	2
	Li_xMnO_2	2
Tunnel	$\alpha\text{-MnO}_2$	1
Rutile	$\beta\text{-MnO}_2$	1
Perovskite	YNiO_3	1
	PrNiO_3	1
Total		27

Table 2. A list of the materials that are used to train and validate the ML model. The last column shows the number of materials. For the olivine-type materials $x = 0, 0.25, 0.50, 0.75, 0$, while for the spinel- and layered-type materials $x = 0, 1$.

our ML model, showcasing its ability to predict Hubbard parameters even with a limited dataset. Despite the size of the dataset, the model exhibits accurate predictions, setting the stage for further refinement and expansion with the upcoming comprehensive investigation.

For each material in our dataset, SC Hubbard U and V parameters are computed using the self-consistent protocol illustrated in fig. 1a. We include all V parameters for Hubbard-active atom pairs whose DFPT values are greater than 0.3 eV, while in Ref. 62 only V for the nearest neighbor couples were included in the training of their ML model. Throughout the iterative process, all intermediate converged occupation matrices and Hubbard parameters are systematically saved. This dataset is then used for training our ENN model. The train-

Chemical element	Number of data points	
	U	V
Ni	396 (124)	67,802 (63,332)
Mn	856 (284)	162,272 (153,232)
Fe	138 (120)	22,511 (21,483)
Total	1,390 (528)	252,585 (238,047)

Table 3. Chemical elements and the total number of data points for both on-site U and inter-site V Hubbard parameters determined using the SC protocol illustrated in fig. 1a. These data points are aggregated across all the materials listed in table 2 that contain the respective chemical element. Numbers in brackets indicate the unique data points after de-duplication (see text).

ing data, as summarized in table 3, is quite substantial when considering the multitude of these first-principles calculations. The dataset for training V comprises approximately seven times more data points than that for training U due to the greater abundance of atom pairs involved in the computation of V , in contrast to the local and consequently sparser nature of U . For each material and chemical element, this data is randomly split, holding back 20% from each material for validation.

In the first-principles calculations, certain input Hubbard parameters (U_{in} and V_{in}) yield a specific ground state and occupation matrices, and the response of the system due to a perturbation through DFPT provides corresponding output Hubbard parameters (U_{out} and V_{out}). This one-to-one correspondence allows our ML model to discern the mapping between input and output Hubbard parameters and the associated intermediate occupation matrices. In addition, it is worth noting that many of the structures encompass symmetry-equivalent sites, and correlations between results from successive self-consistent steps are prevalent. To address this issue, we implement a

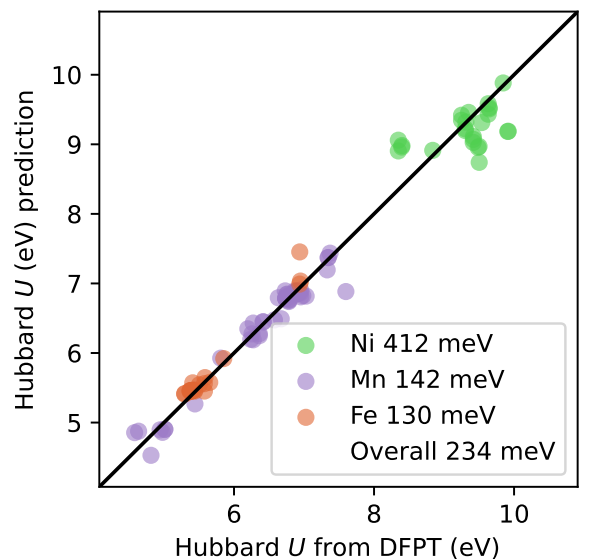
de-duplication procedure aimed at mitigating potential biases in our training data. This involves calculating a symmetry-invariant distance between all pairs of ENN inputs for each atomic species in each material, which is then used to cluster duplicates based on a specified distance threshold (see Sec. S4 in the SI). In random train/validate splits, we sample from these clusters rather than individual data points, ensuring that only one example from each cluster is included in the validation set.

Accuracy of the ML model in predicting the SC Hubbard parameters

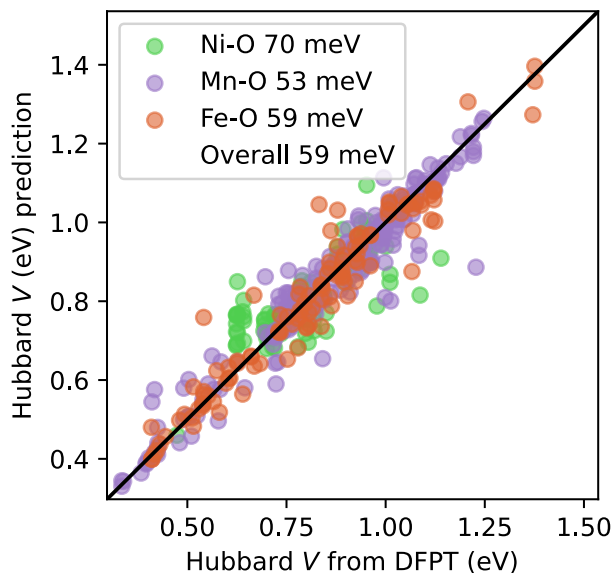
First, we aim to learn the final SC Hubbard parameters for the TM elements across all the materials in our dataset. This is achieved using all attributes listed in table 1 as inputs for our ML model. Figure 3 shows the parity plots obtained for the on-site U and inter-site V Hubbard parameters. The mean absolute relative error (MARE) over all species consistently remains below 3% and 5% for the U and V parameters, respectively (per-species distributions are reported in Sec. S5 in the SI). The result for Hubbard U is particularly promising, considering the relatively small amount of available training data. The higher MARE obtained for V is likely due to the significantly increased number of degrees of freedom in its model, owing to the involvement of pairs of atoms. It is worth noting that in order to attain this accuracy in predicting the U and V values, utilizing a relatively small batch size of 8 – 16 was beneficial in preventing overfitting.

Second, we examine the extent to which our ML model depends upon the input Hubbard parameters for its prediction accuracy. To investigate this, we repeat the same numerical experiment as above, eliminating the input Hubbard parameters (U_{in} and V_{in}) from our model. As detailed in Sec. S6 in the SI, the parity plots closely resemble those in fig. 3. The reduction in accuracy of our ML model resulting from this simplification is relatively small, namely the overall root-mean-square error (RMSE) is increases by 29 and 18 meV for the on-site U and inter-site V , respectively. This finding suggests that the input Hubbard parameters may not be the most critical input attributes for our ML model, and that the input occupation matrices contain sufficient information to make low-error predictions.

Although the model’s relative error is low, it is important to evaluate its impact on downstream properties, such as e.g. voltages in Li-ion battery cathode materials. Table 4 shows a comparison of calculated open-circuit voltage (OCV)¹⁸ within the DFT+ U + V framework, using first-principles SC Hubbard parameters from DFPT and those predicted by our ML model. We find that the differences between the computed and predicted U and V values are less than 0.12 eV for Li_xMnPO_4 and Li_xFePO_4 ($x = 0$ and $x = 1$). Generally, such a small variation in the values of Hubbard parameters has a negligible impact on the vast majority of various physical and chemical properties of materials. The differences observed in the OCV in Table 4 are indeed negligible, indicating the accuracy and reliability of the ML-predicted Hubbard parameters.



(a)



(b)

Figure 3. Parity plots showing the prediction accuracy on an unseen validation dataset, where the energies in the legend are the RMSE categorized by element(s) and the overall RMSE across all elements. All attributes listed in table 1 are used as inputs for the ML model. (a) Hubbard U for 3d states of TM elements, (b) Hubbard V between the TM-3d and O-2p states.

ML model’s performance using a reduced number of iterations in the SC protocol

In the preceding section, we assessed the ML model’s performance in predicting final self-consistent Hubbard parameters using training data that consists of a subset of DFPT calculations from all iterations of the SC protocol (see fig. 1a). However, this approach relies on conducting numerous computationally intensive DFPT

x	Property	Li_xMnPO_4	Li_xFePO_4
0 – 1	Φ (DFPT)	4.205	3.544
	Φ (ML)	4.194	3.544
	$\Delta\Phi$	-0.26%	0.00%
0	m (DFPT)	3.9738	4.1828
	m (ML)	3.9720	4.1832
	Δm	-0.05%	0.01%
1	m (DFPT)	4.7482	3.7388
	m (ML)	4.7486	3.7391
	Δm	0.01%	0.01%

Table 4. Comparison of the open-circuit voltages Φ (in V) and magnetic moments for TM elements (in μ_B) for Li_xMnPO_4 and Li_xFePO_4 computed within DFT+ U + V , with U and V obtained from first principles using DFPT and predicted using the ML model. The voltages are computed using the total energy differences for the Li concentrations $x = 0$ and $x = 1$, while the magnetic moments are computed as the trace of the difference between the spin-up and spin-down occupation matrices.¹⁸ $\Delta\Phi$ and Δm are the relative differences between the voltages and magnetic moments based on DFPT and ML, respectively.

calculations to generate these training data (often 2 – 5 but occasionally up to 10 per material to reach self-consistency). In this experiment, we assess the performance of the model by training on only the first $N_{\text{iter}} - 1$ DFPT result, and asking it to predict the outcome of the next DFPT calculation. This gives an indication of whether the model can be useful in a scenario where a limited number of self-consistent steps are carried out, such as during the early stages of a high-throughput screening study.

Figure 4 shows the average RMSE over all elements as the number of SC iterations used for training N_{iter} increases. The reference data corresponds to RMSE evaluated using DFPT calculations, i.e. excluding the ML component. This RMSE is computed by determining the difference between the Hubbard parameters at the current N_{iter} th and the previous ($N_{\text{iter}} - 1$)th iteration. It is evident that the reference RMSE decreases non-monotonically, which was observed in previous studies,¹⁹ and eventually diminishes at large N_{iter} . It is noteworthy that the optimal N_{iter} for achieving self-consistency in the SC protocol varies for different materials listed in table 2. Therefore, for larger N_{iter} values in fig. 4, fewer data points are available compared to smaller N_{iter} values.

The ML-based RMSE in fig. 4 at the N_{iter} th iteration is computed by training the model on data from all previous $N_{\text{iter}} - 1$ iterations and predicting the Hubbard parameters for the N_{iter} th iteration. Section S7 in the SI contains parity plots for various values of N_{iter} , ranging from 2 to 7, alongside the reference results broken down by element as well as the results for the training set. It is evident from fig. 4 that the ML-based RMSE steadily decreases, and for all N_{iter} values except $N_{\text{iter}} = 6$, it is smaller than the RMSE of the refer-

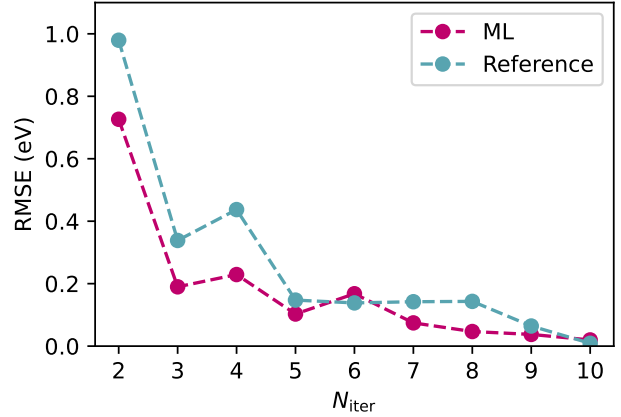


Figure 4. RMSE as a function of the number of iterations N_{iter} in the SC protocol (see fig. 1a). The reference data represents the RMSE obtained from successive DFPT calculations (without ML involvement), whereas the ML data denotes the RMSE resulting from ML predictions for the N_{iter} th iteration based on training the model on all preceding $N_{\text{iter}} - 1$ iterations, with validation conducted using the DFPT data for the N_{iter} th iteration as a reference.

ence dataset. This result shows that our ML model can improve upon a DFPT-based SC result that was terminated early, particularly during the first few iterations, thereby facilitating faster convergence of Hubbard parameters. For instance, the reference value for $N_{\text{iter}} = 2$ indicates that on average, a single-shot DFPT calculation yields Hubbard parameters with an RMSE of ~ 1 eV, while the ML model trained on single-shot data can reduce this error to under 0.8 eV. Incorporating additional N_{iter} iterations in the ML training data leads to steady improvements, although the relative performance compared to the reference gradually diminishes until reaching the floor of the model’s accuracy. This floor is partly determined by the convergence of the underlying DFPT-based Hubbard parameters in the SC protocol, conducted with a tolerance of approximately $\Delta = 0.01 - 0.1$ eV (see fig. 1a). Therefore, the most significant computational savings in predicting the SC Hubbard parameters can be achieved using our ML model, which acts as a surrogate, after only a few iterations in the DFPT-based SC protocol. This substantially reduces the overall computational cost and renders it a feasible approach, particularly for high-throughput screening scenarios where *a priori* training data is unavailable for all materials.

Transferability of the ML model To test the transferability of the model, we isolate training data from the olivines (Li_xMPO_4 with $M = \text{Fe}, \text{Mn}, \text{or } \text{Fe}_{0.5}\text{Mn}_{0.5}$) for which we have calculations at Li concentrations $x = 0, 0.25, 0.5, 0.75, 1$. Within this class of materials, the OS of TM elements Mn and Fe changes from +2 to +3 upon delithiation.⁸⁰ As mentioned earlier, this change of OS is directly reflected in changes to the occupation matrices.¹⁸ Consequently, the Hubbard param-

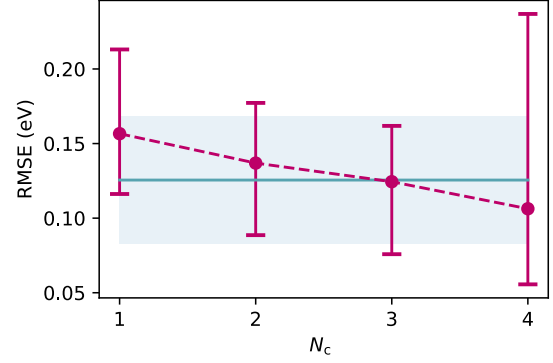
eters for TM elements at different OS also exhibit variation. For instance, the SC Hubbard U parameter for Mn changes from 4.56 to 6.26 eV when transitioning from +2 to +3, while for Fe this change is from 5.29 to 5.43 eV.¹⁸ In addition, in Sec. S8 of the SI we present the distribution of Hubbard U parameters for Fe and Mn ions in the olivines extracted from the DFPT-based SC protocol for various Li concentrations. Our ML model effectively captures these changes in the Hubbard parameters and accurately predicts their values based on the occupation matrices for each TM ion at different Li concentrations.

The outcomes of our numerical experiments are shown in fig. 5. As a reference, we compute the RMSE individually for each material by training the ML model on 80% of the data from all five concentrations and validating it on the remaining 20% of the data after de-duplication. This yields RMSE values of 126, 182, and 420 meV for the Fe, Mn, and mixed Fe-Mn olivines, respectively (see the horizontal lines in fig. 5). Subsequently, we investigate the RMSE values for scenarios in which the ML model is trained on fewer concentrations, denoted as N_c , to assess the sensitivity of the ML model to the amount of the training data and its transferability for predicting Hubbard parameters at other concentrations. To accomplish this, we train the ML model on N_c concentrations and validate it on the remaining $5 - N_c$ concentrations, and then we average out over all possible permutations of the concentrations between the training and validation datasets. The average RMSE values are represented by dots, while the error bars in fig. 5 indicate the maximum and minimum RMSE values resulting from the various permutations. It can be seen that as N_c increases, the average RMSE for each material decreases, reaching values of approximately 106, 301, and 652 meV at $N_c = 4$ for the Fe, Mn, and mixed Fe-Mn olivines, respectively.

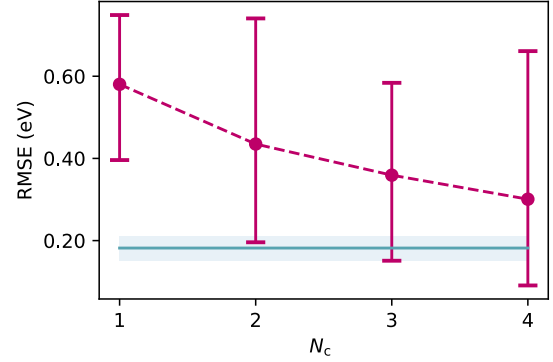
This experiment demonstrates that, depending on the desired accuracy, it is not necessary to include training data from the exact compositions that the model is being evaluated on, and even using examples at one or two concentrations may be sufficient to extrapolate to other parts of the composition range. Given the computational cost of SC calculations, this can lead to a significant speedup, particularly in cases requiring larger supercells and various configurations of Li ion distributions within the structure. Overall, these findings demonstrate the good transferability of our ML model, indicating its potential utility and reliability for predicting Hubbard parameters in materials not included in the model’s training dataset.

DISCUSSION

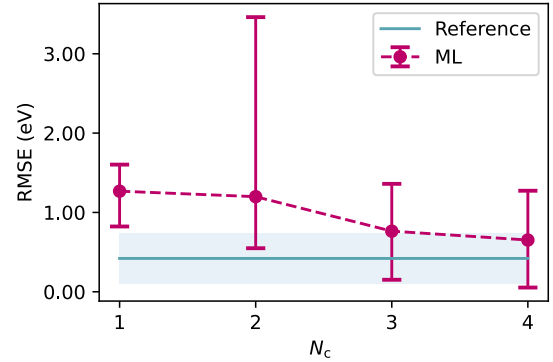
We have introduced a novel equivariant ML model designed for predicting the self-consistent on-site U and inter-site V Hubbard parameters, thereby circumventing the computationally intensive DFPT-based protocols. The model incorporates three input descriptors: Hubbard parameters, inter-atomic distances, and, notably, atomic occupation matrices. The latter



(a) Li_xFePO_4 (Ref. = 0.126 eV)



(b) Li_xMnPO_4 (Ref. = 0.182 eV)



(c) $\text{Li}_x\text{Fe}_{0.5}\text{Mn}_{0.5}\text{PO}_4$ (Ref. = 0.420 eV)

Figure 5. RMSE as a function of N_c (the number of Li concentrations x) for the three olivines: (a) Li_xFePO_4 , (b) Li_xMnPO_4 , and (c) $\text{Li}_x\text{Fe}_{0.5}\text{Mn}_{0.5}\text{PO}_4$. The ML model is trained and validated using N_c and the remaining $5 - N_c$ concentrations, respectively. Error bars indicate the range of RMSE values obtained by considering various permutations of concentrations in the training and validation datasets, the dots represent the average. Reference data is the RMSE computed by training the ML model on 80% of all five concentrations, with validation performed on the remaining 20% after de-duplication. The line represents the mean results over three runs with different random initializations, the confidence interval show the standard deviation.

play a pivotal role in encoding essential information about the electronic structure and local chemical environment within materials. Such an ML model holds significant promise, particularly for high-throughput investigations and large-scale systems, scenarios where DFPT-based approaches become too computationally expensive. Furthermore, the model demonstrates good transferability, rendering it reliable for predicting Hubbard parameters in materials not included in its training dataset, or as a very accurate first guess for further DFPT refinements.

The usage of our ML model is straightforward and entails two DFT-based calculations for a given material. Initially, a ground-state calculation employing DFT+ U + V with initial guesses for U and V (which can be set to zero) is conducted to determine the atomic occupation matrices required as input for the model. Subsequently, a final structural optimization using the model-predicted SC Hubbard parameters yields a self-consistent structural-electronic ground state. The computational cost of these two calculations and a model evaluation is negligible compared to the DFPT-based SC protocol they replace. Furthermore, we have demonstrated that the full SC protocol can be reduced to just a few iterations, which prove adequate for achieving a RMSE within a few percent of the real value.

Unlike other ML models designed for predicting Hubbard parameters,^{28,29,61,62} our model does not rely on experimental data or information from other state-of-the-art computational methods such as GW and hybrid functionals, which possess inherent limitations and specific ranges of applicability. Instead, our model exclusively relies on linear-response theory through DFPT, which provides material-specific Hubbard parameters directly reflecting the local chemistry and OS of TM elements. Notably, our model not only predicts on-site Hubbard U parameters but also inter-site Hubbard V parameters, crucial for materials characterized by significant covalent interactions, an aspect that was disregarded in previous studies.⁸¹ Furthermore, the architecture of our ML model is highly versatile, permitting easy integration of additional inputs and outputs, facilitating exploration of diverse learning tasks beyond learning Hubbard parameters. We expect that similar hybrid ML-accelerated electronic structure methodologies, maintaining accuracy and transferability, will become prevalent, potentially yielding a comparable impact on the field as observed with ML interaction potentials.

Lastly, it is essential to highlight the limitations of the trained models we have presented. These were trained on data generated using a specific computational setup (see below), which must remain exactly the same when the model is applied to other systems. In other words, the U and V values predicted by the model are not transferable across electronic-structure codes and even across different pseudopotentials within the same code.⁸² Furthermore, the training data only encompass Fe, Mn, and Ni with Hubbard U corrections, while V parameters are available for pairs involving these elements and O. Consequently, these models can effectively predict

Hubbard parameters for other materials with Hubbard corrections on these atoms or atom pairs, provided that the model input is generated using identical pseudopotentials, Hubbard projectors, and functional (further elaborated in the methods section). Nevertheless, with a more diverse dataset, the models could be easily extended to accommodate a broader range of compositions. Indeed, ongoing efforts aim to establish a comprehensive database of Hubbard parameters for various TM-containing materials, akin to Ref. 83, thereby significantly broadening the scope of our model to encompass numerous TM elements across diverse OS and chemical environments. Moreover, our model can integrate into automated AiiDA workflows,^{84,85} enabling non-experts to harness it effortlessly and access SC Hubbard parameters with minimal intervention. Consequently, we believe that our ML model represents a significant advancement in expediting materials discovery, design, and understanding based on the DFT+ U + V approach, thereby unlocking new avenues for technological progress and breakthroughs.

METHODS

All calculations are performed using the plane-wave pseudopotential method as implemented in the QUANTUM ESPRESSO distribution.^{86–88} We use the exchange-correlation functional constructed using σ -GGA with the PBEsol prescription,⁸⁹ and the pseudopotentials are taken from the SSSP library v1.1 (efficiency).^{90,91} For metallic ground states, we use Gaussian smearing. To construct the Hubbard projectors, we use atomic orbitals which are orthonormalized using Löwdin’s method.^{92,93} Structural optimizations are performed using DFT+ U + V ⁵⁸ with the Broyden-Fletcher-Goldfarb-Shanno (BFGS) algorithm⁹⁴ and convergence thresholds for the total energy of 10^{-6} Ry, for forces of 10^{-5} Ry/Bohr, and for pressure of 0.5 Kbar. The DFPT calculations of Hubbard parameters are performed using the HP code,⁹⁵ with an accuracy of 0.01 – 0.1 eV for the computed values of U and V . The information about the kinetic-energy cutoff, \mathbf{k} and \mathbf{q} points sampling of the Brillouin zone for each system are detailed in Sec. S9 in the SI. More technical details can be found directly in the source files publicly available through the Materials Cloud Archive (see below).

DATA AVAILABILITY

The data used to produce the results of this work will be available in the Materials Cloud Archive prior to the publication at <https://archive.materialscloud.org>.

CODE AVAILABILITY

The code for the equivariant neural networks is available at <https://github.com/camml-lab/hubbardml/>. Results were generated using the code at git commit d67007e04676741818f5bcebb4373746351b4b3d.

ACKNOWLEDGEMENTS

We thank Francesco Aquilante, Mario Geiger, and Jigyasa Nigam for fruitful discussions. We acknowledge support by the NCCR MARVEL, a National Centre of Competence in Research, funded by the Swiss National Science Foundation (Grant number 205602). This work was supported by a grant from the Swiss National Supercomputing Centre (CSCS) under project ID s1073 (Piz Daint) and ID 465000416 (LUMI-G). This work has been partially supported by MIAI@Grenoble Alpes, (ANR-19-P3IA-0003).

Author contributions statement

M.U. developed and trained ML model architecture; A.Z. wrote data processing code; L.B. and I.T. performed self-consistent calculations of Hubbard parameters; M.U., A.Z., L.B., N.M. and I.T. analysed the results and wrote the manuscript.

References

1. Hohenberg, P. & Kohn, W. Inhomogeneous electron gas. *Phys. Rev.* **136**, B864, DOI: [10.1103/PhysRev.136.B864](https://doi.org/10.1103/PhysRev.136.B864) (1964).
2. Kohn, W. & Sham, L. Self-consistent equations including exchange and correlation effects. *Phys. Rev.* **140**, A1133, DOI: [10.1103/PhysRev.140.A1133](https://doi.org/10.1103/PhysRev.140.A1133) (1965).
3. Perdew, J. & Zunger, A. Self-interaction correction to density-functional approximations for many-electron systems. *Phys. Rev. B* **23**, 5048, DOI: [10.1103/PhysRevB.23.5048](https://doi.org/10.1103/PhysRevB.23.5048) (1981).
4. Kulik, H., Cococcioni, M., Scherlis, D. & Marzari, N. Density Functional Theory in Transition-Metal Chemistry: A Self-Consistent Hubbard U Approach. *Phys. Rev. Lett.* **97**, 103001, DOI: [10.1103/PhysRevLett.97.103001](https://doi.org/10.1103/PhysRevLett.97.103001) (2006).
5. Mori-Sánchez, P., Cohen, A. & Yang, W. Many-electron self-interaction error in approximate density functionals. *J. Chem. Phys.* **125**, 201102, DOI: [10.1063/1.2403848](https://doi.org/10.1063/1.2403848) (2006).
6. Anisimov, V., Zaanen, J. & Andersen, O. Band theory and Mott insulators: Hubbard U instead of Stoner I . *Phys. Rev. B* **44**, 943, DOI: [10.1103/PhysRevB.44.943](https://doi.org/10.1103/PhysRevB.44.943) (1991).
7. Liechtenstein, A., Anisimov, V. & Zaanen, J. Density-functional theory and strong interactions: Orbital ordering in Mott-Hubbard insulators. *Phys. Rev. B* **52**, R5467, DOI: [10.1103/PhysRevB.52.R5467](https://doi.org/10.1103/PhysRevB.52.R5467) (1995).
8. Dudarev, S., Botton, G., Savrasov, S., Humphreys, C. & Sutton, A. Electron-energy-loss spectra and the structural stability of nickel oxide: An LSDA+ U study. *Phys. Rev. B* **57**, 1505, DOI: [10.1103/PhysRevB.57.1505](https://doi.org/10.1103/PhysRevB.57.1505) (1998).
9. Campo Jr, V. L. & Cococcioni, M. Extended DFT+ U + V method with on-site and inter-site electronic interactions. *J. Phys.: Condens. Matter* **22**, 055602, DOI: [10.1088/0953-8984/22/5/055602](https://doi.org/10.1088/0953-8984/22/5/055602) (2010).
10. Tancogne-Dejean, N. & Rubio, A. Parameter-free hybridlike functional based on an extended Hubbard model: DFT+ U + V . *Phys. Rev. B* **102**, 155117, DOI: [10.1103/PhysRevB.102.155117](https://doi.org/10.1103/PhysRevB.102.155117) (2020).
11. Lee, S.-H. & Son, Y.-W. First-principles approach with a pseudohybrid density functional for extended Hubbard interactions. *Phys. Rev. Res.* **2**, 043410, DOI: [10.1103/PhysRevResearch.2.043410](https://doi.org/10.1103/PhysRevResearch.2.043410) (2020).
12. Sun, J., Ruzsinszky, A. & Perdew, J. Strongly Constrained and Appropriately Normed Semilocal Density Functional. *Phys. Rev. Lett.* **115**, 036402, DOI: [10.1103/PhysRevLett.115.036402](https://doi.org/10.1103/PhysRevLett.115.036402) (2015).
13. Bartók, A. & Yates, J. Regularized SCAN functional. *J. Chem. Phys.* **150**, 161101, DOI: [10.1063/1.5094646](https://doi.org/10.1063/1.5094646) (2019).
14. Furness, J., Kaplan, A., Ning, J., Perdew, J. & Sun, J. Accurate and Numerically Efficient r^2 SCAN Meta-Generalized Gradient Approximation. *J. Phys. Chem. Lett.* **11**, 8208, DOI: [10.1021/acs.jpclett.0c02405](https://doi.org/10.1021/acs.jpclett.0c02405) (2020).
15. Adamo, C. & Barone, V. Toward reliable density functional methods without adjustable parameters: The PBE0 model. *J. Chem. Phys.* **110**, 6158, DOI: [10.1063/1.478522](https://doi.org/10.1063/1.478522) (1999).
16. Heyd, J., Scuseria, G. & Ernzerhof, M. Hybrid functionals based on a screened Coulomb potential. *J. Chem. Phys.* **118**, 8207, DOI: [10.1063/1.1564060](https://doi.org/10.1063/1.1564060) (2003).
17. Heyd, J., Scuseria, G. & Ernzerhof, M. Erratum: “Hybrid functionals based on a screened Coulomb potential” [J. Chem. Phys. 118, 8207 (2003)]. *J. Chem. Phys.* **124**, 219906, DOI: [10.1063/1.2204597](https://doi.org/10.1063/1.2204597) (2006).
18. Timrov, I., Aquilante, F., Cococcioni, M. & Marzari, N. Accurate Electronic Properties and Intercalation Voltages of Olivine-type Li-ion Cathode Materials from Extended Hubbard Functionals. *PRX Energy* **1**, 033003, DOI: [10.1103/PRXEnergy.1.033003](https://doi.org/10.1103/PRXEnergy.1.033003) (2022).
19. Timrov, I., Marzari, N. & Cococcioni, M. Self-consistent Hubbard parameters from density-functional perturbation theory in the ultrasoft and projector-augmented wave formulations. *Phys. Rev. B* **103**, 045141, DOI: [10.1103/PhysRevB.103.045141](https://doi.org/10.1103/PhysRevB.103.045141) (2021).
20. Himmetoglu, B., Floris, A., de Gironcoli, S. & Cococcioni, M. Hubbard-corrected DFT energy functionals: The LDA+ U description of correlated systems. *Int. J. Quant. Chem.* **114**, 14, DOI: [10.1002/qua.24521](https://doi.org/10.1002/qua.24521) (2014).
21. Cococcioni, M. & de Gironcoli, S. Linear response approach to the calculation of the effective interaction parameters in the LDA+ U method. *Phys. Rev. B* **71**, 035105, DOI: [10.1103/PhysRevB.71.035105](https://doi.org/10.1103/PhysRevB.71.035105) (2005).

22. Wang, L., Maxisch, T. & Ceder, G. Oxidation energies of transition metal oxides within the GGA+U framework. *Phys. Rev. B* **73**, 195107, DOI: [10.1103/PhysRevB.73.195107](https://doi.org/10.1103/PhysRevB.73.195107) (2006).
23. Kubaschewski, O., Alcock, C. & Spencer, P. *Materials thermochemistry* (Pergamon Press: Elmsford, New York, 1993), 6th edn.
24. Le Bacq, O., Pasturel, A. & Bengone, O. Impact on electronic correlations on the structural stability, magnetism, and voltage of LiCoPO₄ battery. *Phys. Rev. B* **69**, 245107, DOI: [10.1103/PhysRevB.69.245107](https://doi.org/10.1103/PhysRevB.69.245107) (2004).
25. Aykol, M. & Wolverton, C. Local environment dependent GGA+U method for accurate thermochemistry of transition metal compounds. *Phys. Rev. B* **90**, 115105, DOI: [10.1103/PhysRevB.90.115105](https://doi.org/10.1103/PhysRevB.90.115105) (2014).
26. Isaacs, E. & Marianetti, C. Compositional phase stability of strongly correlated electron materials within DFT+U. *Phys. Rev. B* **95**, 045141, DOI: [10.1103/PhysRevB.95.045141](https://doi.org/10.1103/PhysRevB.95.045141) (2017).
27. Hedin, L. New Method for Calculating the One-Particle Green's Function with Application to the Electron-Gas Problem. *Phys. Rev.* **139**, A796, DOI: [10.1103/PhysRev.139.A796](https://doi.org/10.1103/PhysRev.139.A796) (1965).
28. Yu, M., Yang, S., Wu, C. & Marom, N. Machine learning the Hubbard *U* parameter in DFT+U using Bayesian optimization. *npj Comput. Mater.* **6**, 180, DOI: [10.1038/s41524-020-00446-9](https://doi.org/10.1038/s41524-020-00446-9) (2020).
29. Tavadze, P. *et al.* Exploring DFT+U parameter space with a Bayesian calibration assisted by Markov chain Monte Carlo sampling. *npj Comput. Mater.* **7**, 182, DOI: [10.1038/s41524-021-00651-0](https://doi.org/10.1038/s41524-021-00651-0) (2021).
30. Skone, J., Govoni, M. & Galli, G. Self-consistent hybrid functional for condensed systems. *Phys. Rev. B* **89**, 195112, DOI: [10.1103/PhysRevB.89.195112](https://doi.org/10.1103/PhysRevB.89.195112) (2014).
31. Skone, J., Govoni, M. & Galli, G. Nonempirical range-separated hybrid functionals for solids and molecules. *Phys. Rev. B* **93**, 235106, DOI: [10.1103/PhysRevB.93.235106](https://doi.org/10.1103/PhysRevB.93.235106) (2016).
32. Dederichs, P., Blügel, S., Zeller, R. & Akai, H. Ground States of Constrained Systems: Application to Cerium Impurities. *Phys. Rev. Lett.* **53**, 2512, DOI: [10.1103/PhysRevLett.53.2512](https://doi.org/10.1103/PhysRevLett.53.2512) (1984).
33. McMahan, A., Martin, R. & Satpathy, S. Calculated effective Hamiltonian for La₂CuO₄ and solution in the impurity Anderson approximation. *Phys. Rev. B* **38**, 6650, DOI: [10.1103/PhysRevB.38.6650](https://doi.org/10.1103/PhysRevB.38.6650) (1988).
34. Gunnarsson, O., Andersen, O., Jepsen, O. & Zaanen, J. Density-functional calculation of the parameters in the Anderson model: Application to Mn in CdTe. *Phys. Rev. B* **39**, 1708, DOI: [10.1103/PhysRevB.39.1708](https://doi.org/10.1103/PhysRevB.39.1708) (1989).
35. Hybertsen, M., Schlüter, M. & Christensen, N. Calculation of Coulomb-interaction parameters for La₂CuO₄ using a constrained-density-functional approach. *Phys. Rev. B* **39**, 9028, DOI: [10.1103/PhysRevB.39.9028](https://doi.org/10.1103/PhysRevB.39.9028) (1989).
36. Gunnarsson, O. Calculation of parameters in model Hamiltonians. *Phys. Rev. B* **41**, 514, DOI: [10.1103/PhysRevB.41.514](https://doi.org/10.1103/PhysRevB.41.514) (1990).
37. Pickett, W., Erwin, S. & Ethridge, E. Reformulation of the LDA+U method for a local-orbital basis. *Phys. Rev. B* **58**, 1201, DOI: [10.1103/PhysRevB.58.1201](https://doi.org/10.1103/PhysRevB.58.1201) (1998).
38. Solovyev, I. & Imada, M. Screening of Coulomb interactions in transition metals. *Phys. Rev. B* **71**, 045103, DOI: [10.1103/PhysRevB.71.045103](https://doi.org/10.1103/PhysRevB.71.045103) (2005).
39. Nakamura, K., Arita, R., Yoshimoto, Y. & Tsuneyuki, S. First-principles calculation of effective onsite Coulomb interactions of 3d transition metals: Constrained local density functional approach with maximally localized Wannier functions. *Phys. Rev. B* **74**, 235113, DOI: [10.1103/PhysRevB.74.235113](https://doi.org/10.1103/PhysRevB.74.235113) (2006).
40. Shishkin, M. & Sato, H. Self-consistent parametrization of DFT+U framework using linear response approach: Application to evaluation of redox potentials of battery cathodes. *Phys. Rev. B* **93**, 085135, DOI: [10.1103/PhysRevB.93.085135](https://doi.org/10.1103/PhysRevB.93.085135) (2016).
41. Mosey, N. & Carter, E. Ab initio evaluation of Coulomb and exchange parameters for DFT+U calculations. *Phys. Rev. B* **76**, 155123, DOI: [10.1103/PhysRevB.76.155123](https://doi.org/10.1103/PhysRevB.76.155123) (2007).
42. Mosey, N., Liao, P. & Carter, E. Rotationally invariant ab initio evaluation of Coulomb and exchange parameters for DFT+U calculations. *J. Chem. Phys.* **129**, 014103, DOI: [10.1063/1.2943142](https://doi.org/10.1063/1.2943142) (2008).
43. Andriotis, A., Sheetz, R. & Menon, M. LSDA+U method: A calculation of the *U* values at the Hartree-Fock level of approximation. *Phys. Rev. B* **81**, 245103, DOI: [10.1103/PhysRevB.81.245103](https://doi.org/10.1103/PhysRevB.81.245103) (2010).
44. Agapito, L., Curtarolo, S. & Buongiorno Nardelli, M. Reformulation of DFT+U as a Pseudohybrid Hubbard Density Functional for Accelerated Materials Discovery. *Phys. Rev. X* **5**, 011006, DOI: [10.1103/PhysRevX.5.011006](https://doi.org/10.1103/PhysRevX.5.011006) (2015).
45. Springer, M. & Aryasetiawan, F. Frequency-dependent screened interaction in Ni within the random-phase approximation. *Phys. Rev. B* **57**, 4364, DOI: [10.1103/PhysRevB.57.4364](https://doi.org/10.1103/PhysRevB.57.4364) (1998).
46. Kotani, T. *Ab initio* random-phase-approximation calculation of the frequency-dependent effective interaction between 3d electrons: Ni, Fe, and MnO. *J. Phys.: Condens. Matter* **12**, 2413, DOI: [10.1088/0953-8984/12/11/307](https://doi.org/10.1088/0953-8984/12/11/307) (2000).
47. Aryasetiawan, F. *et al.* Frequency-dependent local interactions and low-energy effective models from electronic

- structure calculations. *Phys. Rev. B* **70**, 195104, DOI: [10.1103/PhysRevB.70.195104](https://doi.org/10.1103/PhysRevB.70.195104) (2004).
48. Aryasetiawan, F., Karlsson, K., Jepsen, O. & Schönberger, U. Calculations of Hubbard U from first-principles. *Phys. Rev. B* **74**, 125106, DOI: [10.1103/PhysRevB.74.125106](https://doi.org/10.1103/PhysRevB.74.125106) (2006).
 49. Timrov, I., Marzari, N. & Cococcioni, M. Hubbard parameters from density-functional perturbation theory. *Phys. Rev. B* **98**, 085127, DOI: [10.1103/PhysRevB.98.085127](https://doi.org/10.1103/PhysRevB.98.085127) (2018).
 50. Timrov, I. *et al.* Electronic structure of Ni-substituted LaFeO₃ from near edge x-ray absorption fine structure experiments and first-principles simulations. *Phys. Rev. Res.* **2**, 033265, DOI: [10.1103/PhysRevResearch.2.033265](https://doi.org/10.1103/PhysRevResearch.2.033265) (2020).
 51. Mahajan, R., Kashyap, A. & Timrov, I. Pivotal Role of Intersite Hubbard Interactions in Fe-Doped α -MnO₂. *J. Phys. Chem. C* **126**, 14353, DOI: <https://doi.org/10.1021/acs.jpcc.2c04767> (2022).
 52. Timrov, I., Kotiuga, M. & Marzari, N. Unraveling the effects of inter-site Hubbard interactions in spinel Li-ion cathode materials. *Phys. Chem. Chem. Phys.* **25**, 9061, DOI: [10.1039/d3cp00419h](https://doi.org/10.1039/d3cp00419h) (2023).
 53. Binci, L., Kotiuga, M., Timrov, I. & Marzari, N. Hybridization driving distortions and multiferroicity in rare-earth nickelates. *Phys. Rev. Res.* **5**, 033146, DOI: [10.1103/PhysRevResearch.5.033146](https://doi.org/10.1103/PhysRevResearch.5.033146) (2023).
 54. Haddadi, F., Linscott, E., Timrov, I., Marzari, N. & Gibertini, M. On-site and inter-site Hubbard corrections in magnetic monolayers: The case of FePS₃ and CrI₃. *Phys. Rev. Mater.* **8**, 014007, DOI: [10.1103/PhysRevMaterials.8.014007](https://doi.org/10.1103/PhysRevMaterials.8.014007) (2024).
 55. Bonfà, P. *et al.* Magnetostriction-driven muon localisation in an antiferromagnetic oxide. *Phys. Rev. Lett.* **132**, 046701, DOI: [10.1103/PhysRevLett.132.046701](https://doi.org/10.1103/PhysRevLett.132.046701) (2024).
 56. Gelin, S. *et al.* Ternary oxides of s - and p -block metals for photocatalytic solar-to-hydrogen conversion. *PRX Energy* **3**, 013007, DOI: [10.1103/PRXEnergy.3.013007](https://doi.org/10.1103/PRXEnergy.3.013007) (2024).
 57. Macke, E., Timrov, I., Marzari, N. & Ciacchi, L. C. Orbital-resolved DFT+ U for molecules and solids. *arXiv:2312.13580*.
 58. Timrov, I., Aquilante, F., Binci, L., Cococcioni, M. & Marzari, N. Pulay forces in density-functional theory with extended Hubbard functionals: from nonorthogonalized to orthogonalized manifolds. *Phys. Rev. B* **102**, 235159, DOI: [10.1103/PhysRevB.102.235159](https://doi.org/10.1103/PhysRevB.102.235159) (2020).
 59. Kulik, H. & Marzari, N. Accurate potential energy surfaces with a DFT+ U (R) approach. *J. Chem. Phys.* **135**, 194105, DOI: [10.1063/1.3660353](https://doi.org/10.1063/1.3660353) (2011).
 60. Hsu, H., Umemoto, K., Cococcioni, M. & Wentzcovitch, R. First-principles study for low-spin LaCoO₃ with a structurally consistent Hubbard U . *Phys. Rev. B* **79**, 125124, DOI: [10.1103/PhysRevB.79.125124](https://doi.org/10.1103/PhysRevB.79.125124) (2009).
 61. Cai, G. *et al.* Predicting structure-dependent Hubbard U parameters via machine learning. *Mater. Futur.* **3**, 025601, DOI: [10.1088/2752-5724/ad19e2](https://doi.org/10.1088/2752-5724/ad19e2) (2024).
 62. Yu, W. *et al.* Active Learning the High-Dimensional Transferable Hubbard U and V Parameters in the DFT+ U + V Scheme. *J. Chem. Theory Comput.* **19**, 6425, DOI: [10.1021/acs.jctc.2c01116](https://doi.org/10.1021/acs.jctc.2c01116) (2023).
 63. Batzner, S. *et al.* E(3)-equivariant graph neural networks for data-efficient and accurate interatomic potentials. *Nat. Commun.* **13**, 2453, DOI: [10.1038/s41467-022-29939-5](https://doi.org/10.1038/s41467-022-29939-5) (2022).
 64. Musaelian, A. *et al.* Learning local equivariant representations for large-scale atomistic dynamics. *Nat. Commun.* **14**, 579, DOI: [10.1038/s41467-023-36329-y](https://doi.org/10.1038/s41467-023-36329-y) (2023).
 65. Bartók, A. P., Kondor, R. & Csányi, G. On representing chemical environments. *Phys. Rev. B* **87**, 184115, DOI: [10.1103/PhysRevB.87.184115](https://doi.org/10.1103/PhysRevB.87.184115) (2013).
 66. Musil, F. *et al.* Physics-inspired structural representations for molecules and materials. *Chem. Rev.* **121**, 9759–9815, DOI: [10.1021/acs.chemrev.1c00021](https://doi.org/10.1021/acs.chemrev.1c00021) (2021).
 67. Uhrin, M. Through the eyes of a descriptor: Constructing complete, invertible descriptions of atomic environments. *Phys. Rev. B* **104**, 144110, DOI: [10.1103/PhysRevB.104.144110](https://doi.org/10.1103/PhysRevB.104.144110) (2021).
 68. Batatia, I. *et al.* A foundation model for atomistic materials chemistry. *arXiv:2401.00096* (2023).
 69. Sit, P. H.-L., Car, R., Cohen, M. H. & Selloni, A. Simple, Unambiguous Theoretical Approach to Oxidation State Determination via First-Principles Calculations. *Inorg. Chem.* **50**, 10259, DOI: [10.1021/ic2013107](https://doi.org/10.1021/ic2013107) (2011).
 70. Kondor, R. and Lin, Z. and Trivedi, S. Clebsch-Gordan Nets: a Fully Fourier Space Spherical Convolutional Neural Network. *arXiv:1806.09231* (2018).
 71. Thomas, N. Smidt, T. and Kearnes, S. and Yang, L. and Li, L. and Kohlhoff, K. and Riley, P. Tensor field networks: Rotation- and translation-equivariant neural networks for 3D point clouds. *arXiv:1802.08219* (2018).
 72. Grisafi, A. and Wilkins, D.M. and Willatt, M.J. and Ceriotti, M. Atomic-Scale Representation and Statistical Learning of Tensorial Properties. *ACS Symp. Ser.* **1326**, 1–21, DOI: [10.1021/bk-2019-1326.ch001](https://doi.org/10.1021/bk-2019-1326.ch001) (2019).
 73. Geiger, M. *et al.* e3nn/e3nn: 2022-04-13, <https://zenodo.org/record/6459381#YvDuJ-xBxH4>, DOI: [10.5281/zenodo.3724963](https://doi.org/10.5281/zenodo.3724963).
 74. Merchant, A. *et al.* Scaling deep learning for materials discovery. *Nature* **624**, 80–85, DOI: [10.1038/s41586-023-06735-9](https://doi.org/10.1038/s41586-023-06735-9) (2023).

75. Geiger, M. & Smidt, T. E. e3nn: Euclidean neural networks. *arXiv:2207.09453* (2022).
76. Paszke, A. *et al.* Pytorch: An imperative style, high-performance deep learning library. 8024–8035 (Curran Associates, Inc., 2019).
77. Loshchilov, I. & Hutter, F. Decoupled Weight Decay Regularization. *arXiv:1711.05101* (2019).
78. Chakraborty, A., Dixit, M., Aurbach, D. & Major, D. Predicting accurate cathode properties of layered oxide materials using the SCAN meta-GGA density functional. *npj Comput. Mater.* **4**, 60, DOI: [10.1038/s41524-018-0117-4](https://doi.org/10.1038/s41524-018-0117-4) (2018).
79. Mahajan, R., Timrov, I., Marzari, N. & Kashyap, A. Importance of intersite Hubbard interactions in β -MnO₂: A first-principles DFT+U+V study. *Phys. Rev. Mater.* **5**, 104402, DOI: [10.1103/PhysRevMaterials.5.104402](https://doi.org/10.1103/PhysRevMaterials.5.104402) (2021).
80. Cococcioni, M. & Marzari, N. Energetics and cathode voltages of LiMPO₄ olivines (M =Fe, Mn) from extended Hubbard functionals. *Phys. Rev. Mater.* **3**, 033801, DOI: [10.1103/PhysRevMaterials.3.033801](https://doi.org/10.1103/PhysRevMaterials.3.033801) (2019).
81. Except Ref. 62 which is based on the fitting of U and V to reproduce the results obtained using hybrid functionals, but it does not provide a ML model that can be used to predict the Hubbard parameters for new materials.
82. Kulik, H. & Marzari, N. A self-consistent Hubbard U density-functional theory approach to the addition-elimination reactions of hydrocarbons on bare FeO⁺. *J. Chem. Phys.* **129**, 134314, DOI: [10.1063/1.2987444](https://doi.org/10.1063/1.2987444) (2008).
83. Moore, G. *et al.* High-throughput determination of Hubbard U and Hund J values for transition metal oxides via linear response formalism. *Phys. Rev. Mater.* **8**, 014409 (2024).
84. Huber, S. P. *et al.* AiiDA 1.0, a scalable computational infrastructure for automated reproducible workflows and data provenance. *Sci. Data* **7**, 300, DOI: [10.1038/s41597-020-00638-4](https://doi.org/10.1038/s41597-020-00638-4) (2020).
85. Uhrin, M., Huber, S. P., Yu, J., Marzari, N. & Pizzi, G. Workflows in AiiDA: Engineering a high-throughput, event-based engine for robust and modular computational workflows. *Comput. Mater. Sci.* **187**, 110086, DOI: [10.1016/j.commatsci.2020.110086](https://doi.org/10.1016/j.commatsci.2020.110086) (2021).
86. Giannozzi, P. *et al.* Quantum ESPRESSO: A modular and open-source software project for quantum simulations of materials. *J. Phys.: Condens. Matter.* **21**, 395502, DOI: [10.1088/0953-8984/21/39/395502](https://doi.org/10.1088/0953-8984/21/39/395502) (2009).
87. Giannozzi, P. *et al.* Advanced capabilities for materials modelling with Quantum ESPRESSO. *J. Phys.: Condens. Matter.* **29**, 465901, DOI: [10.1088/1361-648X/aa8f79](https://doi.org/10.1088/1361-648X/aa8f79) (2017).
88. Giannozzi, P. *et al.* Quantum ESPRESSO toward the exascale. *J. Chem. Phys.* **152**, 154105, DOI: [10.1063/5.0005082](https://doi.org/10.1063/5.0005082) (2020).
89. Perdew, J. *et al.* Restoring the Density-Gradient Expansion for Exchange in Solids and Surfaces. *Phys. Rev. Lett.* **100**, 136406, DOI: [10.1103/PhysRevLett.100.136406](https://doi.org/10.1103/PhysRevLett.100.136406) (2008).
90. Prandini, G., Marrazzo, A., Castelli, I. E., Mounet, N. & Marzari, N. Precision and efficiency in solid-state pseudopotential calculations. *npj Comput. Mater.* **4**, 72, DOI: [10.1038/s41524-018-0127-2](https://doi.org/10.1038/s41524-018-0127-2) (2018).
91. The SSSP library of the Materials Cloud: <https://www.materialscloud.org/discover/sssp/table/efficiency>.
92. Löwdin, P.-O. On the Non-Orthogonality Problem Connected with the Use of Atomic Wave Functions in the Theory of Molecules and Crystals. *J. Chem. Phys.* **18**, 365, DOI: [10.1063/1.1747632](https://doi.org/10.1063/1.1747632) (1950).
93. Mayer, I. On Löwdin's method of symmetric orthogonalization. *Int. J. Quant. Chem.* **90**, 63, DOI: [10.1002/qua.981](https://doi.org/10.1002/qua.981) (2002).
94. Fletcher, R. *Practical Methods of Optimization* (Wiley, Chichester, 1987), 2nd edn.
95. Timrov, I., Marzari, N. & Cococcioni, M. HP – A code for the calculation of Hubbard parameters using density-functional perturbation theory. *Comput. Phys. Commun.* **279**, 108455, DOI: [10.24435/materialscloud:v6-zd](https://doi.org/10.24435/materialscloud:v6-zd) (2022).

Supplemental information for “Machine learning Hubbard parameters with equivariant neural networks”

Martin Uhrin^{1,2,*}, Austin Zadoks¹, Luca Binci^{1,3,4}, Nicola Marzari^{1,5}, and Iurii Timrov^{1,5,+}

¹Theory and Simulation of Materials (THEOS), and National Centre for Computational Design and Discovery of Novel Materials (MARVEL), École Polytechnique Fédérale de Lausanne (EPFL), CH-1015 Lausanne, Switzerland

²Université Grenoble Alpes, 1130 Rue de la Piscine, BP 75, 38402 St Martin D’Heres, France

³Department of Materials Science and Engineering, University of California at Berkeley, Berkeley, California 94720, United States

⁴Materials Sciences Division, Lawrence Berkeley National Laboratory, Berkeley, CA, 94720, USA

⁵Laboratory for Materials Simulations (LMS), Paul Scherrer Institut (PSI), CH-5232 Villigen PSI, Switzerland

*Email: martin.uhrin@grenoble-inp.fr

+Email: iurii.timrov@psi.ch

S1 Hubbard parameters from DFPT

In Hubbard-corrected DFT, the values of Hubbard parameters are not known *a priori*, making first-principles calculations of Hubbard parameters essential and highly desirable. We compute U and V through a generalized piecewise linearity condition imposed via linear-response theory,¹ based on DFPT.^{2,3} Within this framework, the Hubbard parameters are defined as:

$$U^I = (\chi_0^{-1} - \chi^{-1})_{II}, \quad (\text{S1})$$

and

$$V^{IJ} = (\chi_0^{-1} - \chi^{-1})_{IJ}, \quad (\text{S2})$$

where χ_0 and χ are the bare and self-consistent susceptibilities, measuring the response of atomic occupations to shifts in the potential acting on individual Hubbard manifolds. χ is defined as

$$\chi_{IJ} = \sum_{m\sigma} \frac{dn_{mm}^{I\sigma}}{d\alpha^J}, \quad (\text{S3})$$

where $n_{mm}^{I\sigma} \equiv n_{mm}^{II\sigma}$ is a short-hand notation for the onsite occupation matrix, α^J is the strength of the perturbation of electronic occupations of the J th site, and it is computed at self-consistency of the DFPT calculation. χ_0 has a similar definition, but it is computed before the self-consistent re-adjustment of the Hartree and exchange-correlation potentials.² The response of the occupation matrix is computed in a unit cell as:

$$\frac{dn_{mm}^{I\sigma}}{d\alpha^J} = \frac{1}{N_{\mathbf{q}}} \sum_{\mathbf{q}} e^{i\mathbf{q}\cdot(\mathbf{R}_I - \mathbf{R}_{I'})} \Delta_{\mathbf{q}}^{s'} n_{mm}^{s\sigma}, \quad (\text{S4})$$

where \mathbf{q} is the wavevector of the monochromatic perturbation, $N_{\mathbf{q}}$ is the total number of perturbations, $\Delta_{\mathbf{q}}^{s'} n_{mm}^{s\sigma}$ is the lattice-periodic response of atomic occupations to a \mathbf{q} -specific monochromatic perturbation. $I \equiv (l, s)$ and $J \equiv (l', s')$, where s and s' are the atomic indices in unit cells while l and l' are the unit cell indices, \mathbf{R}_I and $\mathbf{R}_{I'}$ are the Bravais lattice vectors. The quantities $\Delta_{\mathbf{q}}^{s'} n_{mm}^{s\sigma}$ are computed from the response Kohn-Sham wavefunctions, obtained by solving \mathbf{q} -specific Sternheimer equations. More details about the DFPT approach can be found in Refs. 2, 3. The \mathbf{q} -point mesh must be chosen dense enough to make the atomic perturbations decoupled from their periodic replicas. It is important to recall that the main advantage of DFPT over the traditional linear-response approach¹ is that it does not require the usage of computationally expensive supercells. Finally, it is crucial to remind that the values of the computed Hubbard parameters strongly depend on the type of Hubbard projector functions $\phi_m^I(\mathbf{r})$ used in the definition of the occupation matrix [see Eq.(3) in the main text] and the Hubbard potential. In this work, we use the atomic orbitals orthogonalized using the Löwdin method.^{4,5}

S2 Self-consistent protocol

Here we explain in more detail the self-consistent protocol for computing Hubbard parameters which is illustrated in Fig. 1(a) in the main text. The process is initiated by the selection of the crystal structure, which can be taken from crystal structure databases, and an initial guess for the input Hubbard parameters, U_{in} and V_{in} , which can be set to zero. Following this, a structural optimization is performed using DFT+ $U_{\text{in}}+V_{\text{in}}$, encompassing Hubbard forces and stresses.⁶ Subsequently, a DFPT calculation is performed on the relaxed ground state to obtain the output values of Hubbard parameters, U_{out} and V_{out} . If the input and output Hubbard parameters, as well as the geometry, differ beyond user-specified thresholds, the procedure iterates by updating the input Hubbard parameters and geometry. This iterative cycle continues until convergence is achieved for both the Hubbard parameters and the crystal structure. At the end of this iterative procedure, the final self-consistent (SC) Hubbard parameters, U_{SC} and V_{SC} , are obtained. These parameters are then used for production calculations using DFT+ $U_{\text{SC}}+V_{\text{SC}}$. It is worth noting that the SC cycle can take other forms. For instance, one may keep the geometry fixed and converge the Hubbard parameters through multiple DFPT calculations. Only then is the structure updated, followed by the convergence of Hubbard parameters, and this iteration continues until the SC solution is reached. The self-consistent protocol is crucial as it guides the system toward the ground state where the electronic structure and crystal structure are mutually consistent. Additionally, it is important to mention that this protocol can be adapted for use in the DFT+ U framework by setting inter-site V to zero.

Figure 1(b) in the main text provides an example of applying the self-consistent protocol to LiMnPO₄ in the framework of DFT+ U .⁷ In the first iteration, the Hubbard U parameter for Mn-3d states is approximately 5.08 eV, computed on top of the spin-polarized generalized-gradient approximation (σ -GGA) (PBEsol)⁸ ground state (i.e. $U_{\text{in}} = 0$). However, by the end of the self-consistent protocol, the SC value for U is 4.1 eV — a significant change compared to a “single-shot” calculation (i.e., only the first iteration). The observed change is approximately 1 eV, showing a substantial and impactful adjustment for production calculations. It is important to stress that the output U value after the first iteration strongly depends on the guess of the input U value. Hence, even larger variations may be observed between U values after the first and final iterations. The inter-site V values follow a similar convergence trend.³ Numerous studies have demonstrated that DFT+ $U+V$ calculations with SC values for U and V exhibit remarkable agreement with experiments across various materials and properties.^{7,9-15} The self-consistent protocol typically requires only a few steps in the SC cycle to converge the Hubbard parameters with an accuracy of $\Delta = 0.01$ eV, suitable for the majority of applications.

S3 Spherical harmonic conventions

To be able to use the occupation matrices as calculated by Quantum ESPRESSO (QE) it is necessary to perform a change of basis from their convention to that used by e3nn, the neural network library that we use for generating equivariant learnable functions. The following differences need to be accounted for:

1. QE uses the Condon-Shortley phase convention i.e. the spherical harmonics are defined as

$$Y_{\ell}^m = \begin{cases} (-1)^m \sqrt{2} \sqrt{\frac{2\ell+1}{4\pi}} \frac{(\ell-|m|)!}{(\ell+|m|)!} P_{\ell}^{|m|}(\cos\theta) \sin(|m|\varphi) & \text{if } m < 0 \\ \sqrt{\frac{2\ell+1}{4\pi}} P_{\ell}^m(\cos\theta) & \text{if } m = 0 \\ (-1)^m \sqrt{2} \sqrt{\frac{2\ell+1}{4\pi}} \frac{(\ell-m)!}{(\ell+m)!} P_{\ell}^m(\cos\theta) \cos(m\varphi) & \text{if } m > 0. \end{cases} \quad (\text{S5})$$

while in e3nn the factor of $(-1)^m$ is not absorbed into the definition of Y_{ℓ}^m ,

2. QE uses the convention that for vectors ($\ell = 1$) $Y_1^{-1} = p_y$, $Y_1^0 = p_z$, $Y_1^1 = p_x$ while e3nn uses $Y_1^{-1} = p_x$, $Y_1^0 = p_y$, $Y_1^1 = p_z$, and,
3. QE prints values in the order $m = 0, 1, -1, \dots, l, -l$ while e3nn expects $m = -l, -l+1, \dots, 0, \dots, l-1, l$.¹

For the case of $\ell = 1$ the change of basis from QE to e3nn is simply the permutation-reflection matrix

$$Q_{m'm}^1 = \mathcal{P}_{m'm}^1 Q_{m'm}^1 = \begin{bmatrix} -1 & 0 & 0 \\ 0 & 1 & 0 \\ 0 & 0 & -1 \end{bmatrix} \begin{bmatrix} 0 & 0 & 1 \\ 1 & 0 & 0 \\ 0 & 1 & 0 \end{bmatrix} \quad (\text{S6})$$

¹In addition, QE uses column-vector format as opposed to row-vector as used by Python, however this does not affect the occupation matrices as they are symmetric.

However for $\ell > 1$ the situation is more complicated as the spherical harmonics at a given ℓ are no longer related by a simple permutation (e.g. d_{xy} , d_{yz} , d_z^2 , d_{xy} and $d_{x^2-y^2}$). For these cases, we can use the, so called, Wigner-D matrices:

$$D_{m'm}^{\ell}(\alpha, \beta, \gamma) = \langle lm' | \hat{R}(\alpha, \beta, \gamma) | lm \rangle \quad (\text{S7})$$

where $\hat{R}(\alpha, \beta, \gamma) = e^{-i\alpha J_z} e^{-i\beta J_y} e^{-i\gamma J_z}$ is the rotation operator parameterised by the three Euler angles. By plugging in Q_1 we can get the appropriate rotation matrix at any angular frequency, $Q^{\ell} = D_{m'm}^{\ell}(Q_1)$, which can then be pre-multiplied by $\mathcal{P}^{\ell} = (-1)^m \delta_{m'm}$ to get any Q^{ℓ} . Finally, to make QE's occupation matrices compatible with e3nn we simply perform the transformation:

$$n_{m'm}^{\ell} = Q_{m'm}^{\ell} n_{m'm}^{\ell} (Q_{m'm}^{\ell})^T. \quad (\text{S8})$$

S4 De-duplication procedure

Our ML model treats each Hubbard active site (or pair of sites) as independent inputs. However, a unit cell may contain more than one symmetry-equivalent site leading to near-identical inputs and outputs. This would bias our statistics when evaluating the performance of the model, particularly if a random split of the data ends up putting two or more near-identical inputs into the training and validation splits, respectively, as the model will be trained on data that it is being validated on. To avoid this, before each training run we de-duplicate the data by finding clusters of near-identical inputs and choosing only one example which then (depending on the nature of the numerical experiment) ends up in either the training or validation set.

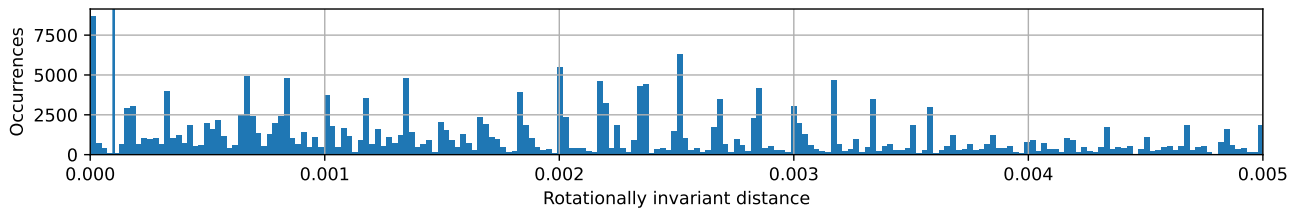
To compare permutationally invariant matrices \mathbf{x}_{ℓ}^i , we calculate the power spectrum distances between pairs of sites:

$$d_{\ell}^{i,IJ} = \sum_k (\mathbf{x}_{\ell}^i)_k^I \cdot (\mathbf{x}_{\ell}^j)_k^J, \quad (\text{S9})$$

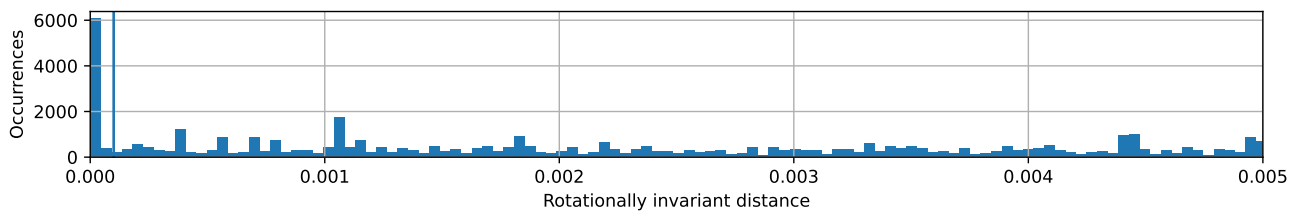
where i can be 1 or 2 (see Eqs. (4) and (5) in the main text), ℓ is the angular momentum of the manifold, k labels each irrep tensor in the spherical harmonic basis, while I and J label the atomic sites. We calculate $d_{\ell}^{i,IJ}$ for all pairs of inputs (grouped by species) and form clusters from all data points that are within the thresholds defined in table S1. The similarity threshold for power spectrum distances was chosen by considering the histogram of distances plotted in fig. S1 and choosing a value just above the large peak near zero. This peak should capture the identical electronic occupations with the minimum to its right separating it from the meaningfully distinguishable configurations.

Attribute	Similarity threshold
U_{in}	10^{-3} eV
V_{in}	10^{-3} eV
$d_{\ell}^{1,IJ}$	10^{-4}
$d_{\ell}^{2,IJ}$	10^{-4}
r_{IJ}	4×10^{-3} Å

Table S1. Similarity thresholds for each of the input attributes provided to the ML model. U_{in} and V_{in} are the input on-site and inter-site Hubbard parameters, respectively, \mathbf{x}_{ℓ}^1 and \mathbf{x}_{ℓ}^2 are the tensors defined in Eqs. (5) and (6) in the main text, and r_{IJ} is the interatomic distance between species I and J .



(a) Distance analysis for \mathbf{x}_ℓ^1



(b) Distance analysis for \mathbf{x}_ℓ^2

Figure S1. Analysis of the symmetry-invariant distance distribution for the two permutationally invariant tensors, \mathbf{x}_ℓ^1 and \mathbf{x}_ℓ^2 . The vertical line represents the chosen threshold for defining two occupation matrices as identical.

S5 Relative error distributions

Figure S2 shows the results for predicting SC Hubbard parameters relative to the values from DFPT. Taking Hubbard U as an example, this is calculated as $\sum_i^N |U_{\text{out}}^i - \tilde{U}_{\text{out}}^i| / U_{\text{out}}$, where the sum runs over all N validation results and the predicted value is indicated with a tilde. Given that the range of Hubbard parameters can vary depending on the element, this gives us a consistent way to assess the global performance of the model. For both Hubbard U and V the trend is similar, with Fe and Mn showing similar mean relative errors, while that of Ni is consistently higher. This may be due to the fact that Ni has a relatively wide range of Hubbard parameters (compared to Fe), but we have less training data than for Mn, which also has a much larger spread of self-consistent parameter values.

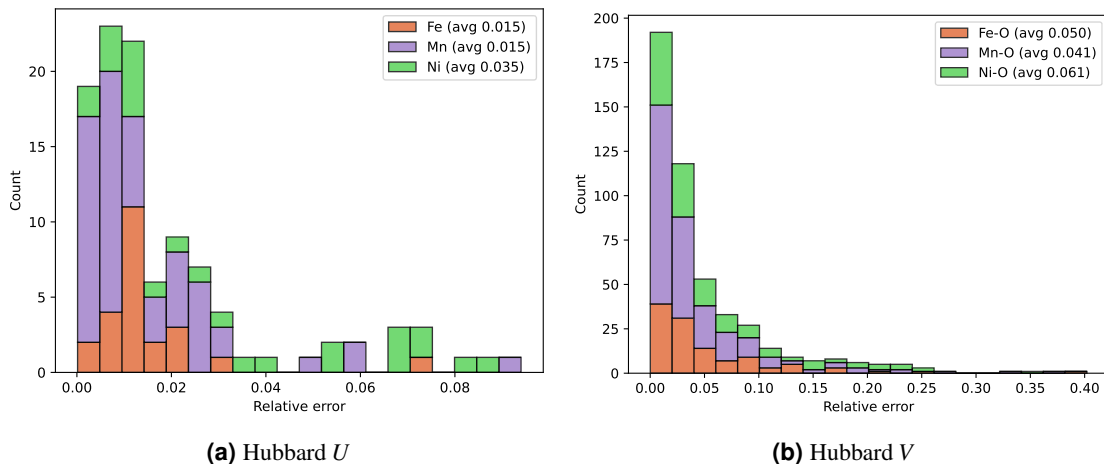


Figure S2. Validation results for predicting final SC Hubbard parameters plotted as a histogram of errors relative to the values from DFPT.

S6 ML model without Hubbard parameters as inputs

Figure S3 shows the parity plots using our ML model when excluding the input Hubbard parameters from the list of input attributes. This numerical test demonstrates that the Hubbard parameters may not be the most critical input attributes for our ML model.

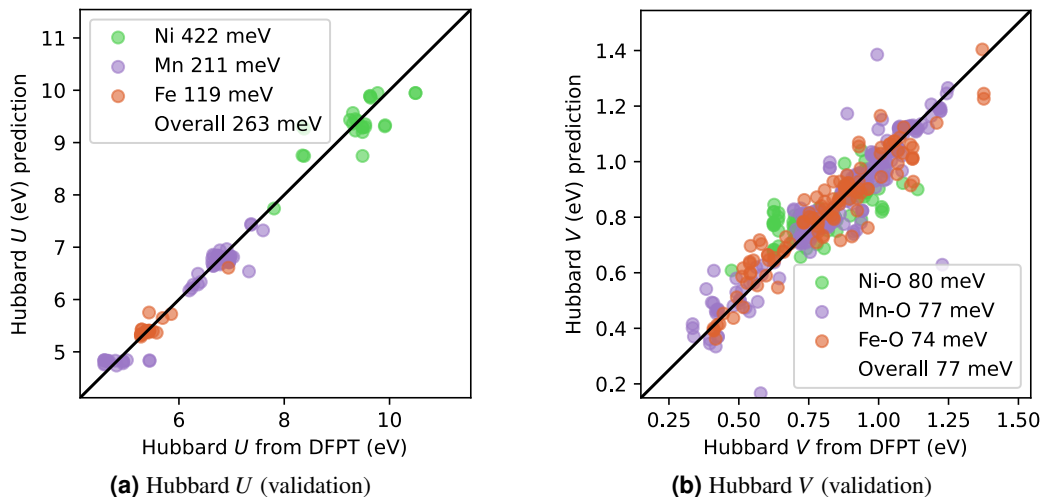


Figure S3. Parity plots showing the prediction accuracy on an unseen validation dataset, where the energies in the legend are the RMSE categorized by element(s) and the overall RMSE across all elements. All attributes listed in Table 1 in the main text (except the input Hubbard parameters) are used as inputs for the ML model. (a) Hubbard U for 3d states of TM elements, (b) Hubbard V between the TM-3d and O-2p states.

S7 RMSE and parity plots at different number of iterations N

Figure S4 show results plotted in fig. 4 of the main article, with the addition of results from the training set. As can be seen, the RMSE on the training results never reach zero as we use early stopping to terminate training when the validation loss starts to increase. In contrast, the validation root-mean-square error (RMSE) gradually at higher N_{iter} as there are fewer and fewer materials with unconverged Hubbard parameters.

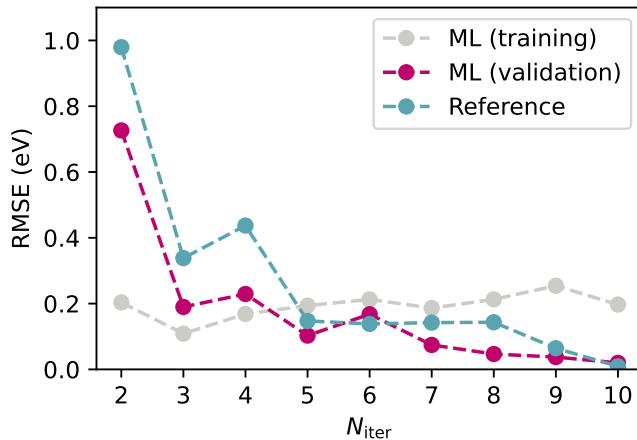


Figure S4. RMSE as a function of the number of iterations N_{iter} in the SC protocol. The reference data represents the RMSE obtained from successive DFPT calculations (without ML involvement), whereas the ML data denotes the RMSE resulting from ML predictions for the N_{iter} -th iteration based on training the model on all preceding $N_{\text{iter}} - 1$ iterations, with validation conducted using the DFPT data for the N_{iter} -th iteration as a reference.

Shown below are parity plots corresponding to a model that was trained on the first $N - 1$ linear-response calculations, and asked to predict the Hubbard U value for the current iteration N , the “target” is always the actual results from performing the linear-response calculation. The reference plots use the LR result from the previous iteration as the “prediction”. In this way, we can assess if the model can learn to improve upon the result obtained from a limited number of DFPT calculations.

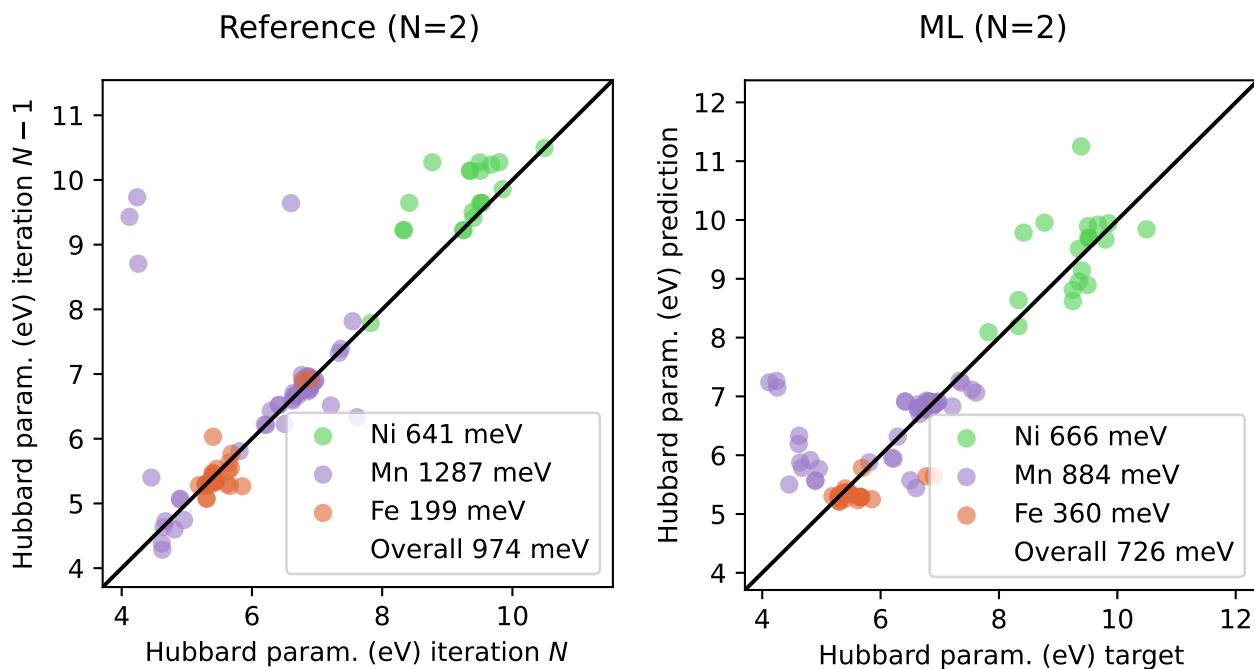


Figure S5. Second linear response step.

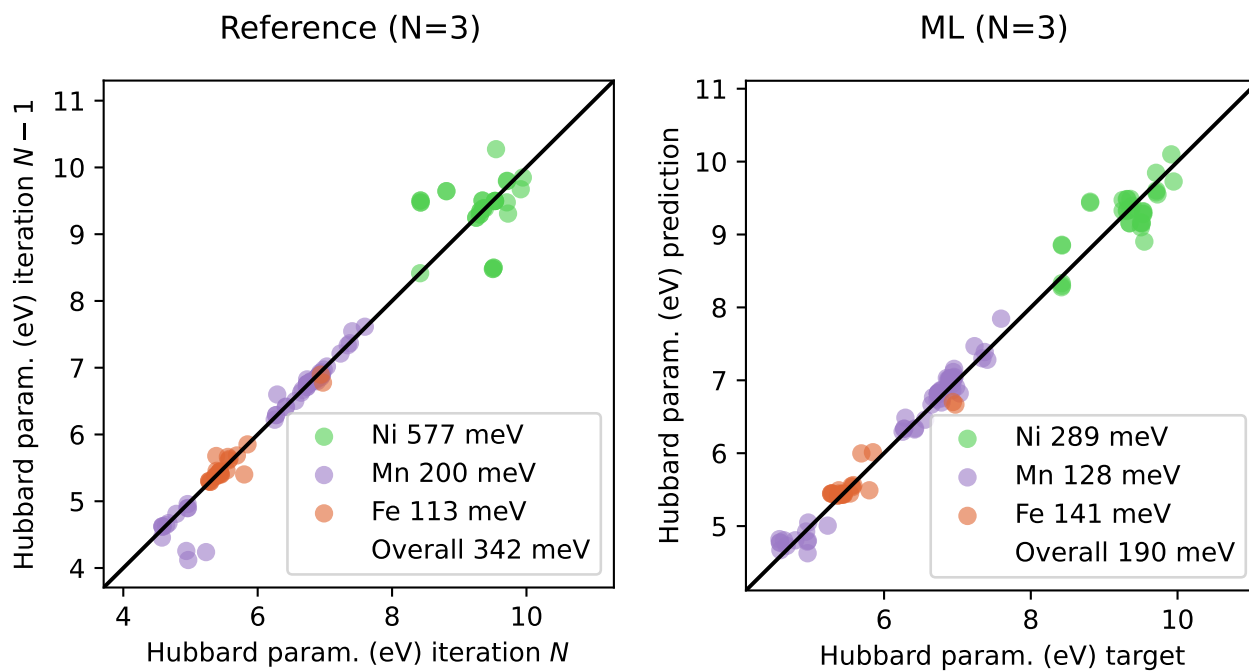


Figure S6. Third linear response step.

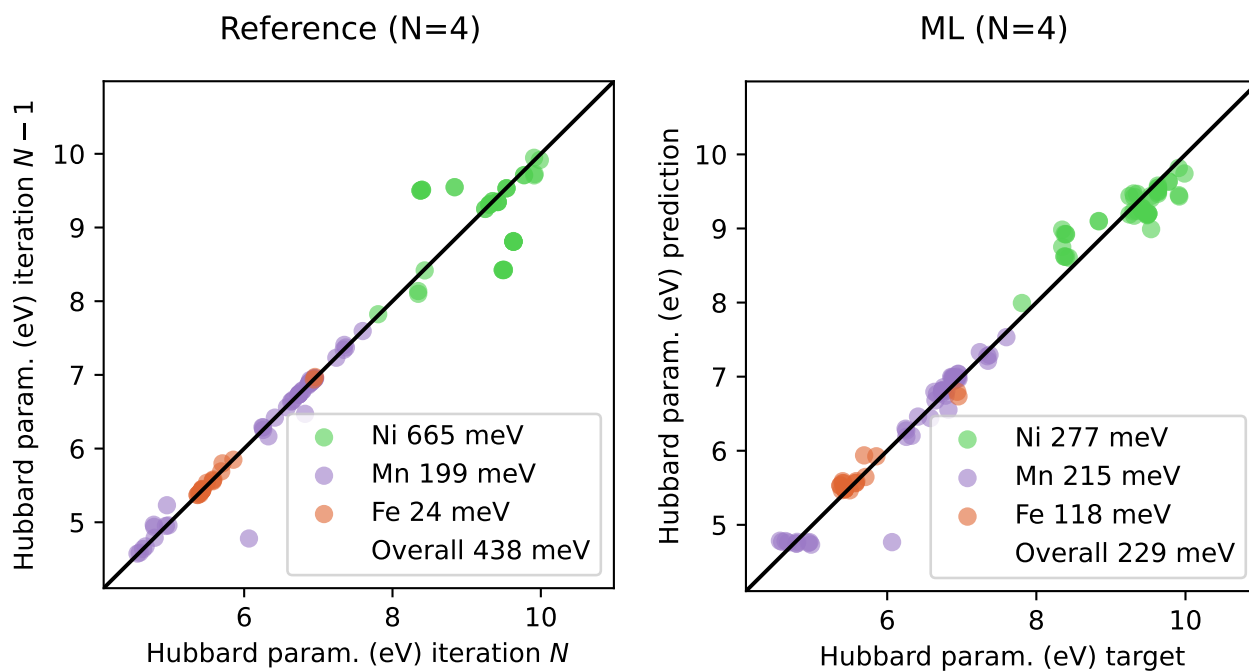


Figure S7. Fourth linear response step.

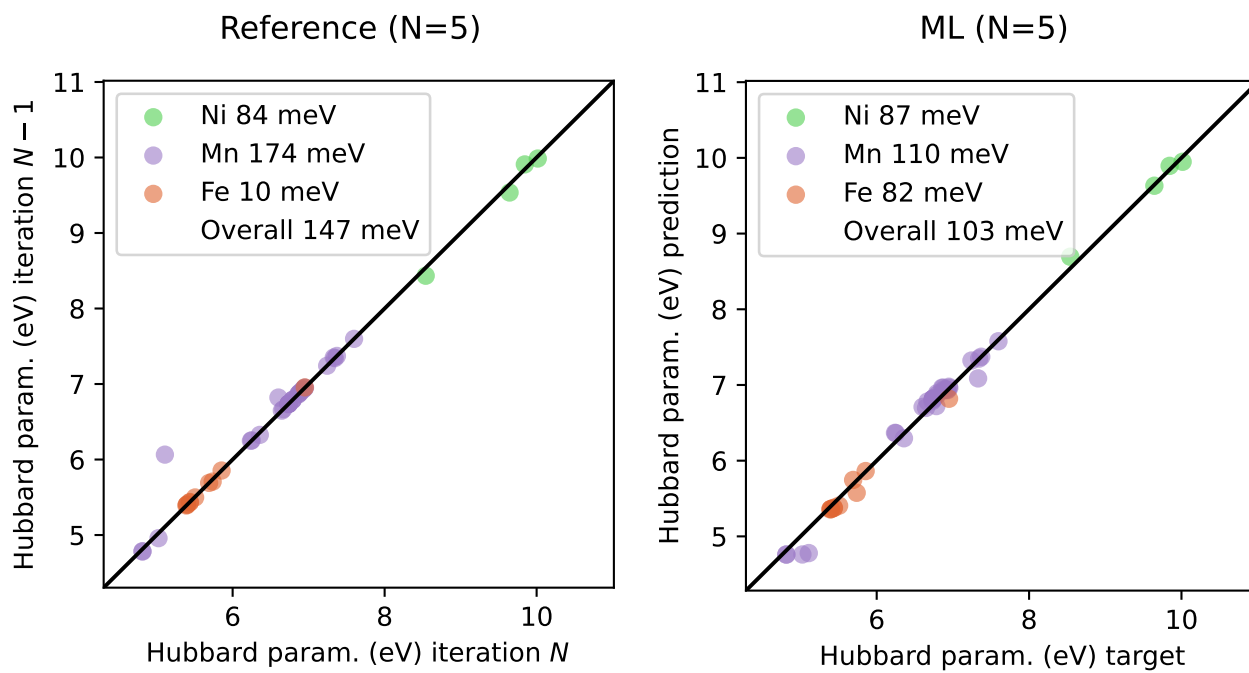


Figure S8. Fifth linear response step.

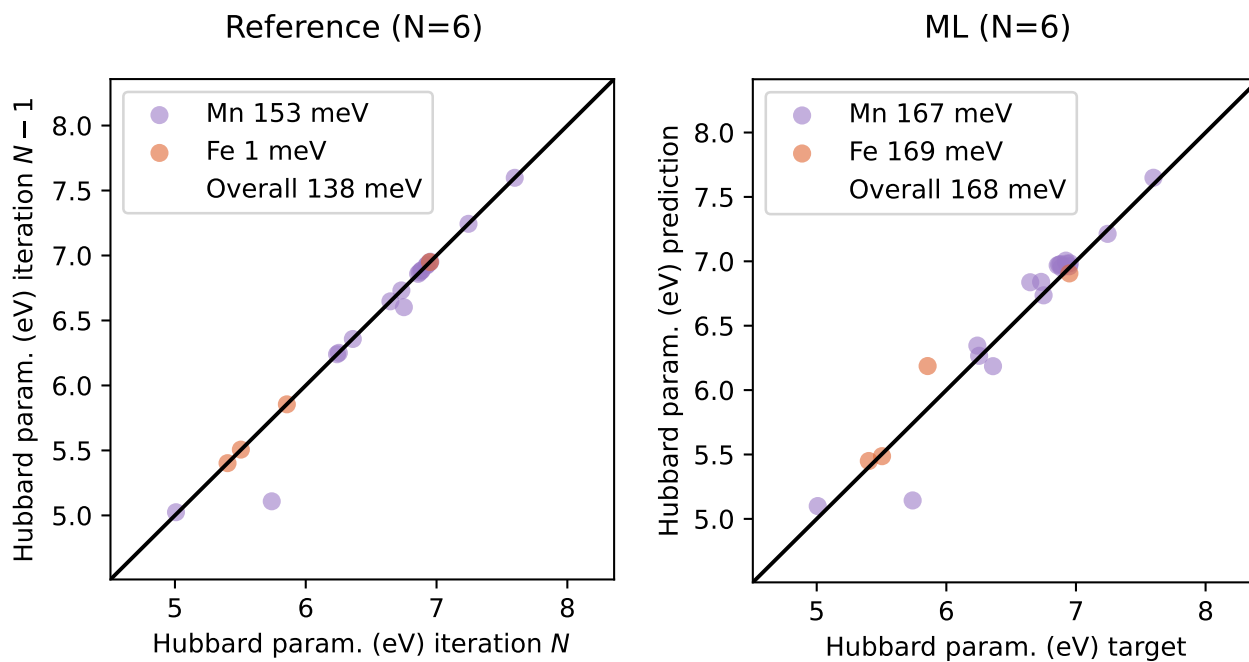


Figure S9. Sixth linear response step.

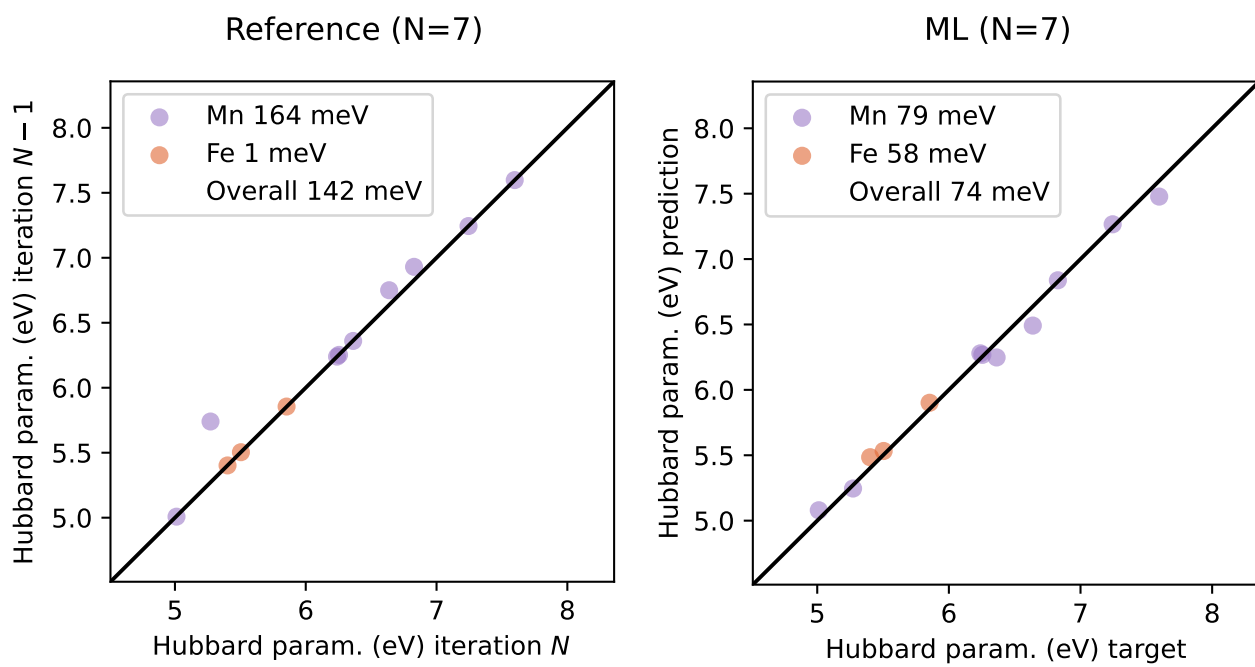


Figure S10. Seventh linear response step.

S8 Olivines linear-response Hubbard U distribution

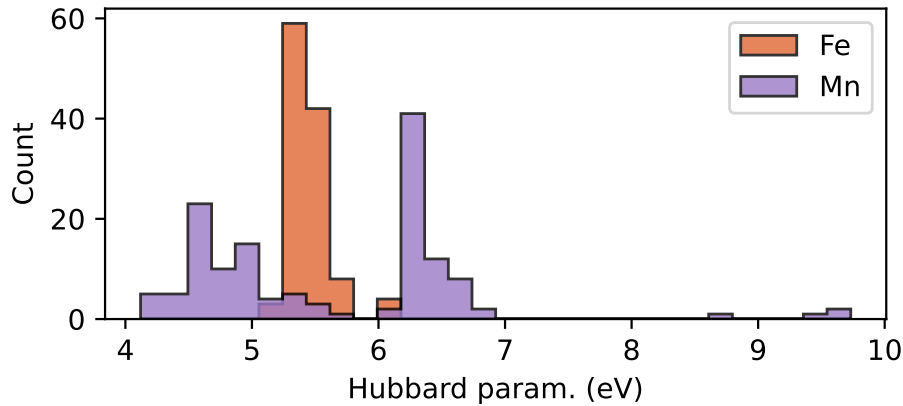


Figure S11. Distribution of Hubbard U values obtained from DFPT calculations during a self-consistent procedure. Notably, the distribution of Mn parameters varies significantly more than that of Fe, with two distinct peaks corresponding to the +2 and +3 oxidation states.

S9 Additional computational details

Material	Number of atoms	Structural optimization		DFPT calculation of Hubbard parameters		
		$E_{\text{cut}}^{\psi} / E_{\text{cut}}^{\rho}$ (Ry)	\mathbf{k} mesh	$E_{\text{cut}}^{\psi} / E_{\text{cut}}^{\rho}$ (Ry)	\mathbf{k} mesh	\mathbf{q} mesh
Li_xFePO_4	24 – 28	90/1080	$5 \times 10 \times 10$	65/780	$3 \times 4 \times 5$	$1 \times 2 \times 3$
Li_xMnPO_4	24 – 28	90/1080	$5 \times 10 \times 10$	65/780	$3 \times 4 \times 5$	$1 \times 2 \times 3$
$\text{Li}_x\text{Fe}_{0.5}\text{Mn}_{0.5}\text{PO}_4$	24 – 28	90/1080	$5 \times 10 \times 10$	65/780	$3 \times 4 \times 5$	$1 \times 2 \times 3$
$\text{Li}_x\text{Mn}_2\text{O}_4$	48 – 56	90/1080	$6 \times 6 \times 6$	65/780	$4 \times 4 \times 4$	$2 \times 2 \times 2$
$\text{Li}_x\text{Mn}_{1.5}\text{Ni}_{0.5}\text{O}_4$	48 – 56	90/1080	$6 \times 6 \times 6$	65/780	$4 \times 4 \times 4$	$2 \times 2 \times 2$
Li_xNiO_2	3 – 4	90/1080	$18 \times 18 \times 10$	65/780	$8 \times 8 \times 4$	$4 \times 4 \times 2$
Li_xMnO_2	3 – 4	90/1080	$18 \times 18 \times 10$	65/780	$8 \times 8 \times 4$	$4 \times 4 \times 2$
α - MnO_2	24 – 25	90/1080	$4 \times 4 \times 12$	60/720	$2 \times 2 \times 6$	$1 \times 1 \times 3$
β - MnO_2	48	90/1080	$4 \times 4 \times 6$	60/720	$2 \times 2 \times 4$	$1 \times 1 \times 2$
YNiO_3						
b-type	40	50/400	$5 \times 8 \times 6$	50/400	$5 \times 8 \times 6$	$1 \times 2 \times 2$
ferro	40	50/400	$8 \times 8 \times 6$	50/400	$8 \times 8 \times 6$	$2 \times 2 \times 2$
s-type	40	50/400	$5 \times 8 \times 6$	50/400	$5 \times 8 \times 6$	$1 \times 2 \times 2$
s-type-true	40	50/400	$5 \times 8 \times 6$	50/400	$5 \times 8 \times 6$	$1 \times 2 \times 2$
t-type	40	50/400	$5 \times 8 \times 6$	50/400	$5 \times 8 \times 6$	$1 \times 2 \times 2$
t-type-true	40	50/400	$5 \times 8 \times 6$	50/400	$5 \times 8 \times 6$	$1 \times 2 \times 2$
PrNiO_3						
b-type	80	50/400	$4 \times 8 \times 3$	50/400	$4 \times 8 \times 3$	$1 \times 2 \times 1$
ferro	20	50/400	$8 \times 8 \times 6$	50/400	$8 \times 8 \times 6$	$2 \times 2 \times 2$
s-type	80	50/400	$4 \times 8 \times 3$	50/400	$4 \times 8 \times 3$	$1 \times 2 \times 1$
t-type	80	50/400	$4 \times 8 \times 3$	50/400	$4 \times 8 \times 3$	$1 \times 2 \times 1$

Table S2. A list of the materials that are used to train and validate the ML model, together with the kinetic-energy cutoff for the wavefunctions (E_{cut}^{ψ}) and charge density (E_{cut}^{ρ}), the sizes of the \mathbf{k} - and \mathbf{q} -point meshes used for the structural optimization and DFPT calculation of Hubbard parameters. Multiple sizes of the \mathbf{k} - and \mathbf{q} -point meshes may have been used to accelerate calculations at the beginning of the self-consistent cycle; only the parameters used in the final iteration are reported here.

References

1. Cococcioni, M. & de Gironcoli, S. Linear response approach to the calculation of the effective interaction parameters in the LDA+U method. *Phys. Rev. B* **71**, 035105, DOI: [10.1103/PhysRevB.71.035105](https://doi.org/10.1103/PhysRevB.71.035105) (2005).
2. Timrov, I., Marzari, N. & Cococcioni, M. Hubbard parameters from density-functional perturbation theory. *Phys. Rev. B* **98**, 085127, DOI: [10.1103/PhysRevB.98.085127](https://doi.org/10.1103/PhysRevB.98.085127) (2018).
3. Timrov, I., Marzari, N. & Cococcioni, M. Self-consistent Hubbard parameters from density-functional perturbation theory in the ultrasoft and projector-augmented wave formulations. *Phys. Rev. B* **103**, 045141, DOI: [10.1103/PhysRevB.103.045141](https://doi.org/10.1103/PhysRevB.103.045141) (2021).
4. Löwdin, P.-O. On the Non-Orthogonality Problem Connected with the Use of Atomic Wave Functions in the Theory of Molecules and Crystals. *J. Chem. Phys.* **18**, 365, DOI: [10.1063/1.1747632](https://doi.org/10.1063/1.1747632) (1950).
5. Mayer, I. On Löwdin's method of symmetric orthogonalization. *Int. J. Quant. Chem.* **90**, 63, DOI: [10.1002/qua.981](https://doi.org/10.1002/qua.981) (2002).
6. Timrov, I., Aquilante, F., Binci, L., Cococcioni, M. & Marzari, N. Pulay forces in density-functional theory with extended Hubbard functionals: from nonorthogonalized to orthogonalized manifolds. *Phys. Rev. B* **102**, 235159, DOI: [10.1103/PhysRevB.102.235159](https://doi.org/10.1103/PhysRevB.102.235159) (2020).
7. Timrov, I., Aquilante, F., Cococcioni, M. & Marzari, N. Accurate Electronic Properties and Intercalation Voltages of Olivine-type Li-ion Cathode Materials from Extended Hubbard Functionals. *PRX Energy* **1**, 033003, DOI: [10.1103/PRX-Energy.1.033003](https://doi.org/10.1103/PRX-Energy.1.033003) (2022).
8. Perdew, J. *et al.* Restoring the Density-Gradient Expansion for Exchange in Solids and Surfaces. *Phys. Rev. Lett.* **100**, 136406, DOI: [10.1103/PhysRevLett.100.136406](https://doi.org/10.1103/PhysRevLett.100.136406) (2008).
9. Ricca, C., Timrov, I., Cococcioni, M., Marzari, N. & Aschauer, U. Self-consistent DFT+U+V study of oxygen vacancies in SrTiO₃. *Phys. Rev. Res.* **2**, 023313, DOI: [10.1103/PhysRevResearch.2.023313](https://doi.org/10.1103/PhysRevResearch.2.023313) (2020).
10. Floris, A. *et al.* Hubbard-corrected density functional perturbation theory with ultrasoft pseudopotentials. *Phys. Rev. B* **101**, 064305, DOI: [10.1103/PhysRevB.101.064305](https://doi.org/10.1103/PhysRevB.101.064305) (2020).
11. Mahajan, R., Timrov, I., Marzari, N. & Kashyap, A. Importance of intersite Hubbard interactions in β -MnO₂: A first-principles DFT+U+V study. *Phys. Rev. Mater.* **5**, 104402, DOI: [10.1103/PhysRevMaterials.5.104402](https://doi.org/10.1103/PhysRevMaterials.5.104402) (2021).
12. Zhou, J.-J. *et al.* *Ab Initio* Electron-Phonon Interactions in Correlated Electron Systems. *Phys. Rev. Lett.* **127**, 126404, DOI: [10.1103/PhysRevLett.127.126404](https://doi.org/10.1103/PhysRevLett.127.126404) (2021).
13. Mahajan, R., Kashyap, A. & Timrov, I. Pivotal Role of Intersite Hubbard Interactions in Fe-Doped α -MnO₂. *J. Phys. Chem. C* **126**, 14353, DOI: <https://doi.org/10.1021/acs.jpcc.2c04767> (2022).
14. Timrov, I., Kotiuga, M. & Marzari, N. Unraveling the effects of inter-site Hubbard interactions in spinel Li-ion cathode materials. *Phys. Chem. Chem. Phys.* **25**, 9061, DOI: [10.1039/d3cp00419h](https://doi.org/10.1039/d3cp00419h) (2023).
15. Binci, L., Kotiuga, M., Timrov, I. & Marzari, N. Hybridization driving distortions and multiferroicity in rare-earth nickelates. *Phys. Rev. Res.* **5**, 033146, DOI: [10.1103/PhysRevResearch.5.033146](https://doi.org/10.1103/PhysRevResearch.5.033146) (2023).